nature communications

Article

https://doi.org/10.1038/s41467-025-61560-0

YY1 enhances HIF-1α stability in tumor-associated macrophages to suppress anti-tumor immunity of prostate cancer in mice

Received: 24 July 2024

Accepted: 26 June 2025

Published online: 07 July 2025

Check for updates

Wenchao Li[1,16], SaiSai Chen[1,2,16], Jian Lu[3,16], Weipu Mao[1,16], Shiya Zheng[4,16], Minhao Zhang[5,16], Tiange Wu[1], Yurui Chen[1], Kai Lu[1], Chunyan Chu[6], Chuanjun Shu[7], Yue Hou[8], Xue Yang[9], Naipeng Shi[10], Zhijun Chen[11], Lihua Zhang[6], Lei Zhang[1], Rong Na[12,17], Ming Chen[1,17], Shenghong Ju[9] ✉, Dingxiao Zhang[13] ✉, Yi Ma[14] ✉ & Bin Xu[1,15] ✉

Immune checkpoint therapy for prostate cancer (PCa), a classic 'immune-cold' tumor characterized by an immunosuppressive tumor microenvironment, failed previously in clinical trials, but the underlying causes remain elusive. Here we find that YY1$^+$, immunosuppressive macrophages aggregate in the hypoxic areas of PCa. Mechanistically, hypoxia promotes the phase separation of YY1 in the nucleus, where YY1 binds to NUSAP1 and promotes the SUMOylation, phase separation and stabilization of HIF-1α. Either myeloid-specific conditional knockout of YY1 or a treatment with tenapanor for decreasing the YY1–NUSAP1–HIF-1α interaction impairs subcutaneous PCa tumor formation in mouse prostate tumor models. Lastly, a first-generation tetrahedral DNA nanostructure based on the proteolysis targeting chimera technique, termed YY1-DcTAC, allows targeting and degrading YY1 in tumor-associated macrophages for inducing antitumor effects and CD8$^+$ T cell tumor infiltration in mouse tumor models. In summary, our findings underscore the pivotal role of YY1 in the hypoxia/HIF-1α pathway in tumor-associated macrophages and support the targeting of YY1 for treating PCa.

Prostate cancer (PCa) is one of the most prevalent malignancies affecting men globally[1]. Despite the ability of androgen deprivation therapy to significantly impede disease progression, a considerable number of patients still experience metastasis or develop castration resistance, ultimately resulting in fatalities[2]. Immune checkpoint therapy (ICT) has demonstrated promising and durable antitumor effects in late-stage patients with certain tumors[3]. ICT promotes T-cell-mediated antitumor immunity by reactivating endogenous T cells "braked" by immune checkpoint molecules. However, PCa has been recognized as an "immune-cold" tumor that exhibits immunosuppressive characteristics and sparse T-cell infiltration[4,5]. Clinical trials in PCa patients have shown poor responsiveness to ICT treatment. These circumstances highlight the importance of investigating the PCa tumor microenvironment (TME) and identifying novel therapeutic targets.

Solid tumors are characterized by a hypoxic microenvironment[6], which can promote malignant proliferation, invasion, and metastasis by modulating antitumor immunity[7,8]. HIF-1α, a pivotal transcription factor with oxygen regulatory activity in the classic hypoxia-inducible factor (HIF) signaling pathway, regulates the tumor-specific immune response by promoting immune suppressive cell infiltration and activating multiple downstream signaling pathways and gene targets[9,10]. Studies have highlighted the propensity of hypoxic environments to attract infiltrating macrophages[11]. Macrophages, the crucial component of the TME, have been established as a predominant immune cell subtype in most immune-cold tumors[12–14]. In various tumor types, including PCa, breast cancer, and melanoma, infiltration of tumor-associated macrophages (TAMs) is significantly correlated with poor prognosis and tumor progression[15–17]. Mechanistically, TAMs can

A full list of affiliations appears at the end of the paper. ✉e-mail: jsh@seu.edu.cn; zdx1980@hnu.edu.cn; yima@cpu.edu.cn; njxbseu@seu.edu.cn

https://doi.org/10.1038/s41467-025-61560-0

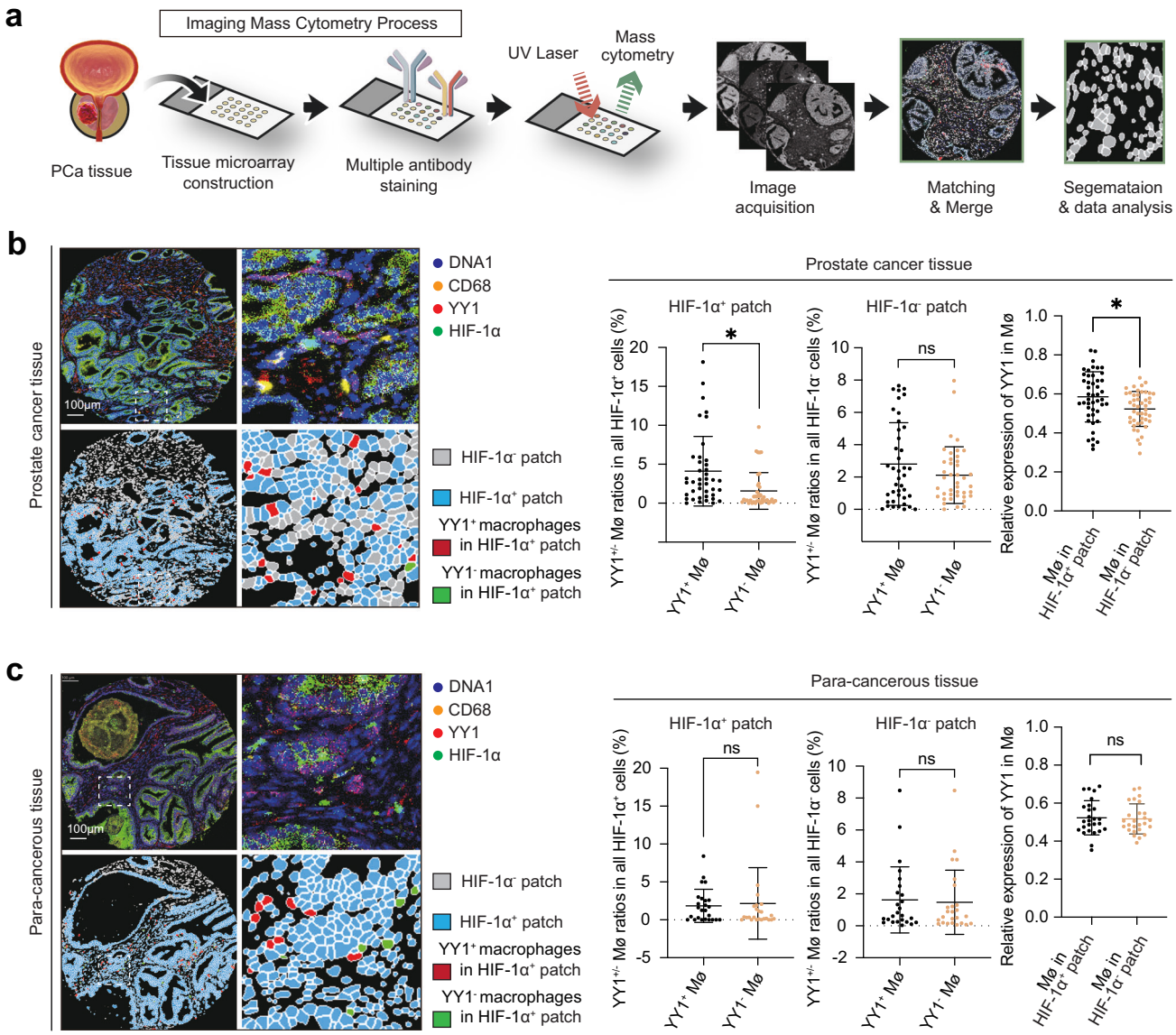

Fig. 1 | YY1⁺ macrophages accumulate in hypoxic tumor tissues. a Schematic diagram showing the process of imaging mass cytometry (IMC) using prostate tissue. IMC of the indicated markers in prostate cancer (PCa) patient tumors (**b**) and para-cancerous tissues (**c**). Pathchs were defined as containing at least 10 cells with a maximum distance of 15 μm between cells involved. Adjacent regions were merged together for downstream analysis. The expression of the marker was normalized using *z*-score, and a threshold of 0.5 was selected. Dot plots showing the ratio of YY1⁺ or YY1⁻ macrophages and the relative YY1 expression of macrophages in HIF-1α⁺ or HIF-1α⁻ patches. The representative plot and analysis are based on 46 tumor samples and 26 para-cancerous tissues. Dot plots present the mean values ± SD, and the *p* values are calculated using a two-tailed *t*-test. The *p* values of left, middle, and right plots of (**b**) are 0.002, 0.160, and 0.009, respectively; The *p* values of left, middle, and right plots of (**c**) are 0.759, 0.798, and 0.820, respectively. $^{*}P < 0.05$, ns $P > 0.05$. Source data are provided as a Source Data file. Mø macrophage.

suppress the antitumor T-cell response by inducing tissue fibrosis, producing multiple immunosuppressive cytokines and chemokines, and decreasing the tumoral infiltration of CD8⁺ T cells[18,19].

In this study, we investigate the role of TAMs expressing high levels of Yin Yang 1 (YY1) in the PCa hypoxic zones, revealing that YY1 induces phase separation and stabilization of HIF-1α within macrophage nuclei via its interaction with nucleolar and spindle-associated protein 1 (NUSAP1). Additionally, we demonstrate that either disrupting the YY1–NUSAP1–HIF-1α interaction using tenapanor or degrading YY1 in macrophages using a tetrahedral DNA nanostructure exhibits robust antitumor properties in a mouse model of PCa and enhances the infiltration of CD8⁺ T cells. These findings provide insights into the role of YY1 in TAMs and highlight potential avenues for PCa immunotherapy.

Results

YY1⁺ macrophages accumulate in hypoxic PCa tissues

Imaging mass cytometry (IMC) was used to analyze prostate tissue microarrays comprising 46 PCa tissues and 26 adjacent noncancerous tissues (Fig. 1a). The hypoxia marker HIF-1α, the macrophage marker CD68, the transcription factor YY1, and the cell nuclear marker DNA1 were used for analysis. A discernible cellular landscape within PCa tissues emerged amidst the intricate spatial orchestration of cell subtypes and transcription factor expression profiles, particularly within hypoxic regions marked by the HIF-1α patch, which refers to the patch where HIF-1α expression is highly concentrated and forms contiguous regions. Notably, a significantly greater percentage of YY1⁺ macrophages than YY1⁻ macrophages was detected within these hypoxic regions (Fig. 1b). Interestingly, no substantial differences in infiltration

were observed between $YY1^+$ or $YY1^-$ macrophages within the hypoxic zones of adjacent noncancerous tissues (Fig. 1c), suggesting a context-specific role for YY1 in the tumor setting.

Moreover, our investigation extended to areas lacking HIF-1α expression (HIF-1α-negative patch), where the positivity rate of YY1 in macrophages within nonhypoxic regions exhibited no significant difference, neither in the tumor center nor adjacent noncancerous tissues (Fig. 1b, c). Additionally, in PCa tumor tissues, macrophages within HIF-1α-positive patches exhibited significantly higher average expression levels of YY1 compared to those in HIF-1α-negative patches. In contrast, no significant difference was observed in peritumoral tissues (Fig. 1b, c). Overall, the infiltration of YY1-expressing macrophages in hypoxic PCa tissues highlights their potential relevance in responding to hypoxia.

Hypoxia enhances YY1 phase separation by inducing its tyrosine phosphorylation in macrophages

To further investigate the response of macrophages to hypoxia, we utilized either authentic hypoxia (1% O_2 and 5% CO_2) or cobalt chloride ($CoCl_2$) to induce hypoxia in vitro in THP-1 cells. Interestingly, we observed the accumulation of punctate YY1 particles within the cell nucleus under hypoxic conditions, which could be attenuated by the phase separation inhibitor 1,6-hexanediol (1,6-Hex) (Fig. 2a, Supplementary Fig. 1a). Additionally, we also observed via the immunofluorescence assay punctate nuclear aggregation of YY1 in $CD68^+$ cells derived from human PCa tissues (Supplementary Fig. 1b). The droplet fission phenomenon observed for the recombinant YY1 protein in living cells indicated that these punctate structures may exhibit characteristics related to phase-separated droplets (Supplementary Fig. 1c). The formation of phase-separated droplets has been shown to participate in the cellular response to physical stimuli or stress and typically relies on the presence of intrinsically disordered protein regions (IDRs)[20]. Here, we predicted through the Predictor of Natural Disordered Regions (PONDR) website that YY1 contains a lengthy N-terminal IDR segment (Supplementary Fig. 1d). Confocal microscopy analysis of living cells constructed with the YY1-IDR-EGFP or YY1-non-IDR-EGFP plasmid revealed that the phase separation ability of YY1-IDR-EGFP, but not that of YY1-non-IDR-EGFP, increased under hypoxic conditions (Supplementary Fig. 1e). Furthermore, we conducted a time-gradient experiment involving hypoxia and reoxygenation in THP-1 cells. With the prolonged duration of hypoxia (0–4 h under 1% O_2 or 0–8 h under $CoCl_2$), the density of droplets progressively increased, eventually returning to baseline levels following 120 min of reoxygenation (back to 21% O_2 condition or normal culture medium) (Fig. 2b, Supplementary Fig. 1f).

To investigate the mechanisms underlying the abovementioned phenotypes, we evaluated the expression of YY1 under hypoxia and found that neither the duration of authentic hypoxia nor the concentrations or exposure times of $CoCl_2$ altered the expression level of YY1 (Fig. 2c, d, Supplementary Fig. 1g, h). Accumulating evidence suggests that the phosphorylation of proteins enhances their phase separation[21,22]; thus, we further investigated the impact of hypoxia on YY1 protein phosphorylation. First, using a panphosphospecific antibody, we revealed that hypoxia augments the expression of phosphorylated YY1, in which the bacterial alkaline phosphatase, a nonspecific phosphatase, was used as a negative control (Fig. 2e, Supplementary Fig. 1i, j). Sodium orthovanadate (Na_3VO_4), a commonly used protein phosphatase inhibitor, not only enhanced the expression of panphosphorylated YY1 (Fig. 2e, Supplementary Fig. 1j) but also facilitated the formation of phase separation droplets of YY1 (Fig. 2f) under normoxia. Serine and tyrosine are frequently reported phosphorylation sites of YY1 (p-Ser and p-Tyr), and we observed that YY1 p-Tyr but not p-Ser levels significantly increased under hypoxia (Fig. 2g, Supplementary Fig. 1k–m). In previous studies, Src family kinases were revealed to be important mediators of YY p-Tyr[23]. In this study, we revealed that SU6656, a selective Src family kinase inhibitor, mitigated YY1 hypoxia-induced phosphorylation and phase separation (Fig. 2h, Supplementary Fig. 1n). These findings suggest that hypoxia augments YY1-mediated phase separation by promoting YY1 tyrosine phosphorylation.

To elucidate the specific sites of hypoxia-induced YY1 p-Tyr, we strategically engineered six tyrosine residues within YY1 into two distinct mutant groups, each fused with EGFP: YY1-mut1 (sites Y8F and Y383F) and YY1-mut2 (sites Y145F, Y185F, Y251F, and Y254F), based on their respective locations within the YY1-non-IDR or YY1-IDR domains (Supplementary Fig. 1d). Interestingly, YY1-mut2 (mutations at the p-Tyr site within the YY1-IDR region) but not YY1-mut1 (mutations in the YY1-non-IDR domain) effectively inhibited the hypoxia-induced increase in the p-Tyr level (Fig. 2i, Supplementary Fig. 1o). Morphological assessments also revealed that YY1-mut2 effectively mitigated the enhancement of phase separation induced by Na_3VO_4 or hypoxia (Fig. 2j).

Furthermore, to determine the tyrosine kinases responsible for the hypoxia-induced phosphorylation of YY1, we intersected the mass spectrometry (MS) results of YY1-immunoprecipitated (IP) proteins with a reported RNA-sequencing (RNA-seq) data from hypoxia-induced macrophages (GSE16099) and a list of known tyrosine kinases (Fig. 2k). One Src family kinase, Lyn, was subsequently identified. Through protein co-IP and cellular immunofluorescence assays, we further confirmed an increased interaction between YY1 and Lyn in hypoxia-induced THP-1 cells, and their colocalization within the nucleus was enhanced under hypoxic conditions (Fig. 2l, m). In addition, silencing Lyn via small interfering RNA (siRNA) markedly impeded the formation of YY1 droplets under hypoxic conditions (Fig. 2n, Supplementary Fig. 1p). Briefly, our investigation revealed that hypoxia promotes the aggregation of YY1 into nuclear puncta by inducing YY1 phosphorylation, with Lyn emerging as a pivotal kinase mediating this process.

Moreover, the YY1 C-terminal segment (comprising amino acids 296–414) constitutes a highly conserved DNA-binding region that houses four zinc-finger motifs (amino acids 296–320, 325–347, 353–377, and 383–407)[24]. Despite our previous finding that silencing p-Tyr sites (145, 185, 251, 254) reduced droplet formation but kept YY1 nuclear-localized (Fig. 2j), here we found that silencing the first YY1 zinc-finger motif (amino acids 296–320) within the functional YY1-IDR and DNA-binding region, designated as $YY1^{\Delta 296-320}$-EGFP, not only nearly abolishes phase separation droplet formation but also disperses YY1 into the cytoplasm (Supplementary Fig. 1q). Conversely, the general silencing of the other three motifs ($YY1^{\Delta 321-414}$-EGFP) did not have a notable impact on the formation of phase-separated droplets (Supplementary Fig. 1q). Consistent with a recent report that showed deletion of the zinc-finger domain in YY1 inhibits the formation of nuclear droplets and leads to even distribution of YY1 in both the nucleus and cytoplasm[25], our research further clarifies that the first segment (amino acids 296–320) of the four zinc fingers may be a key to this process. Collectively, our findings underscore the critical roles of the p-Tyr sites (145, 185, 251, 254) and DNA-binding regions (amino acids 296–320) within the YY1-IDR domain in mediating hypoxia-induced YY1 phase separation.

YY1 stabilizes HIF-1α by inhibiting its ubiquitination

To further investigate the mechanistic processes underlying the function of YY1 in macrophages under hypoxic conditions, we conducted RNA-seq analysis of macrophages overexpressing YY1 and intersected the results with the reported RNA-seq dataset from hypoxia-induced macrophages (GSE16099). In this overlap, we identified a set of 193 genes that are commonly upregulated in both conditions (Fig. 3a). Notably, despite the relatively low proportion of overlapping genes compared to the total number of genes in each group, the intersecting gene set is significantly enriched for the HIF-1

https://doi.org/10.1038/s41467-025-61560-0

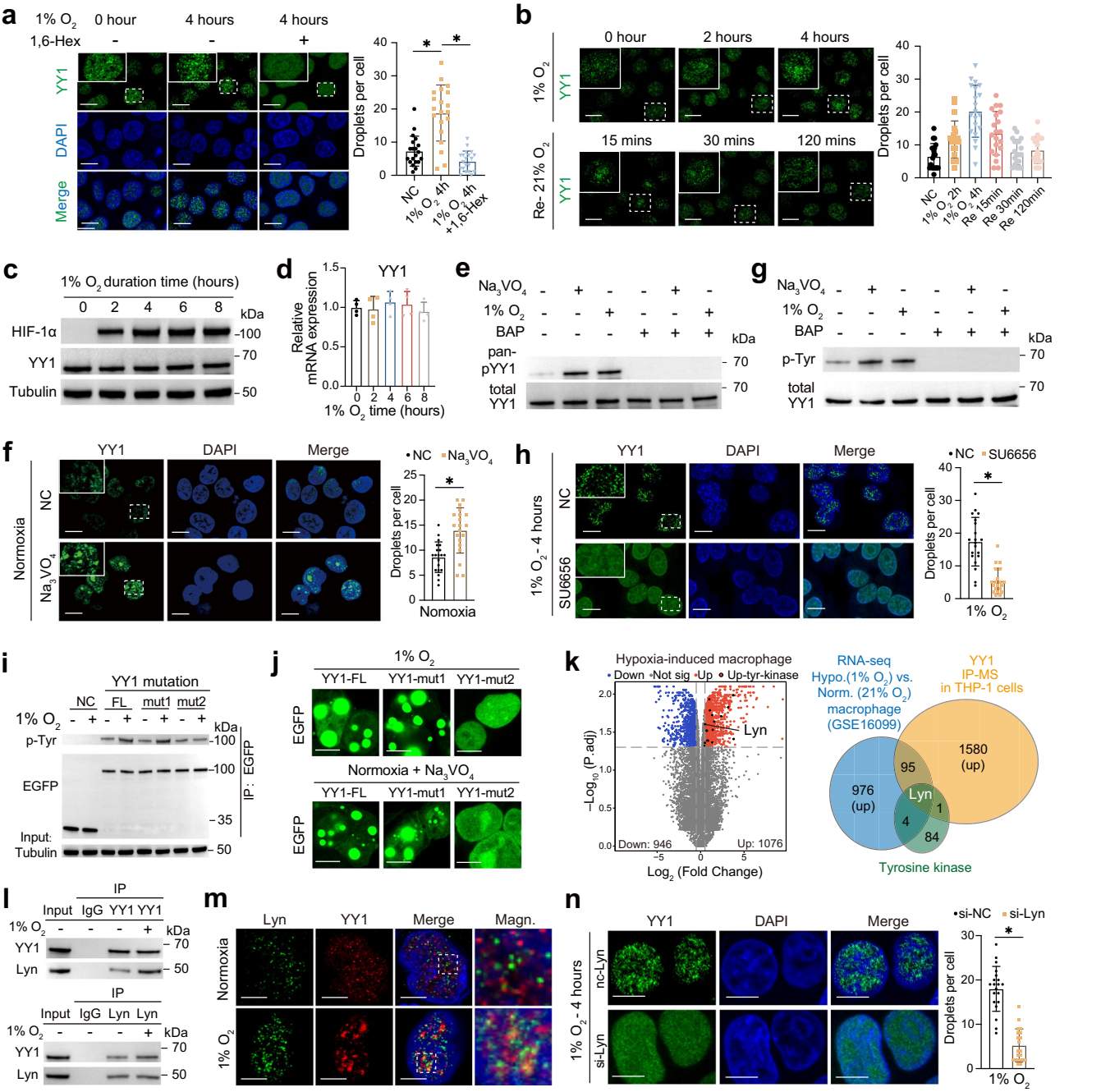

Fig. 2 | Hypoxia enhances YY1 phase separation by inducing YY1 tyrosine phosphorylation in macrophages. a Immunofluorescence staining in THP-1 cells subjected to 1% O_2 and/or 1,6-hexanediol. The *p* values were calculated using both two-tailed *t*-test ($P = 0.017$ and $P < 0.001$) and one-way ANOVA followed by Tukey test ($P < 0.001$). **b** The localization of YY1 was observed by immunofluorescence after hypoxia with 1% O_2 or reoxygenation with 21% O_2. **c** Western blot of HIF-1α and YY1 in THP-1 cells under 1% O_2 hypoxia. **d** qRT–PCR showing the relative RNA expression of *YY1* in THP-1 cells under 1% O_2 hypoxia. **e** Western blot analysis using an anti-phosphorylated YY1 antibody to detect YY1-immunoprecipitated proteins. **f** Immunofluorescence staining in THP-1 cells treated with Na_3VO_4 or control solution under normal oxygen conditions ($P < 0.001$). **g** Western blot analysis using a tyrosine phosphorylation antibody to detect YY1-immunoprecipitated protein. The bacterial alkaline phosphatase was used as a negative control. **h** Immunofluorescence staining in THP-1 cells treated with SU6656 or control solution under 1% O_2 hypoxia ($P < 0.001$). **i** Western blot analysis using a tyrosine phosphorylation antibody to detect EGFP immunoprecipitated from YY1 full-length (YY1-FL), YY1 mutation 1 (YY1-mut1, including amino acid sites 8 and 383), and YY1 mutation 2 (YY1-mut2, including amino acids 145, 185, 251, and 254)-transfected THP-1 cells. **j** Immunofluorescence of YY1-FL-, YY1-mut1- and YY1-mut2-transfected THP-1 cells. **k** The left volcano plot illustrates the differentially expressed genes in the indicated RNA-seq (two-tailed t-test and adjusted with Benjamini and Hochberg method). The right panel shows the overlap indicated to identify Lyn. **l**, **m** Co-IP and immunofluorescence of YY1 and Lyn from 1% O_2 hypoxia- or normoxia-induced THP-1 cells. **n** Immunofluorescence of the indicated markers in THP-1 cells under 1% O_2 hypoxia ($P < 0.001$). All the immunofluorescence data were analyzed, and twenty cells randomly selected from three repeated groups were counted. Scale bar, 5 μm. Bar graphs (**a**, **b**, **d**, **f**, **h**, **n**) present mean values ± SD, and the *p* values are calculated using a two-tailed *t*-test. * $P < 0.05$. Source data are provided as a Source Data file. 1,6-Hex 1,6-hexanediol, BAP bacterial alkaline phosphatase.

https://doi.org/10.1038/s41467-025-61560-0

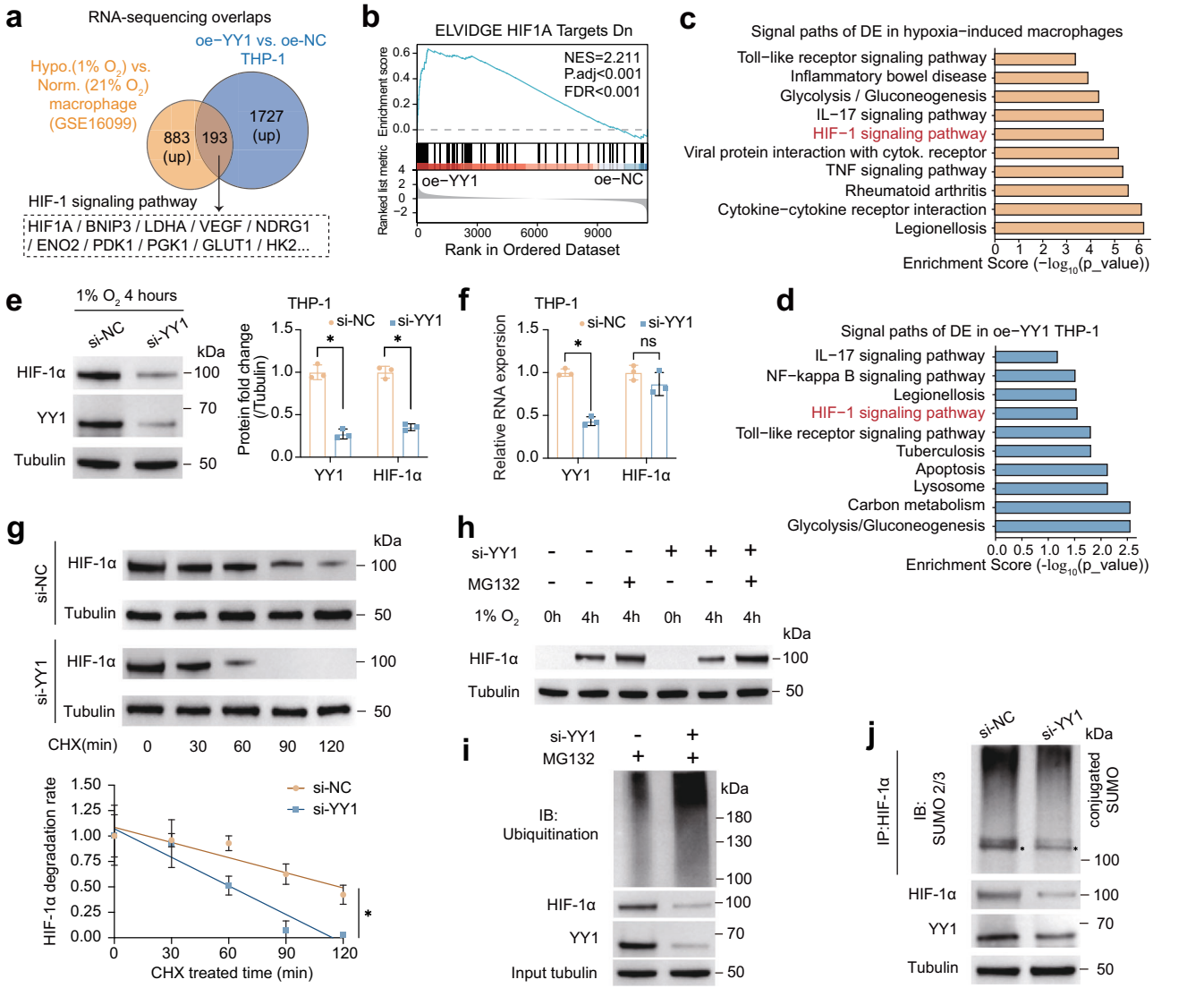

Fig. 3 | YY1 stabilizes HIF-1α by promoting its SUMOylation and inhibiting its ubiquitination. a Venn diagram depicting the overlap between two datasets: (1) RNA-seq analysis comparing oe-YY1 and oe-NC THP-1 cells, and (2) a previously reported RNA-seq dataset from hypoxia-induced macrophages (GSE16099). **b** GSEA analysis of the HIF-1A targets DN set, comparing RNA-seq data from oe-YY1 THP-1 cells to nc-YY1 THP-1 cells. NES and *p* value are indicated (phenotype permutation test). **c**, **d** Gene ontology analysis of enriched signaling pathways in oe-YY1 or hypoxia-induced THP-1 cells when compared to control cells (hypergeometric test and corrected with Benjamini & Hochberg adjustment). **e** Western blot showing the expression of HIF-1α and YY1 in 1% O_2 hypoxia-induced THP-1 cells transfected with siYY1 or the normal control. Samples calculated are from the same experiment, and the blots were processed in parallel ($n = 3$ independent experiments, $P < 0.001$, $P < 0.001$, respectively). **f** qRT–PCR showing the expression of *YY1* and *HIF-1α* in THP-1 cells ($n = 3$ independent experiments, $P < 0.001$, $P = 0.220$, respectively). **g** Western blot of HIF-1α expression in 1% O_2 hypoxia-induced THP-1 cells treated with cycloheximide (n = 3 independent experiments). The lower panel presents mean values ± SD at each time point (linear regression between the two datasets using two-tailed *t*-test, $P < 0.001$). **h** Western blot of HIF-1α expression in THP-1 cells treated with MG132 and/or 1% O_2 hypoxia. **i**, **j** Immunoprecipitation of HIF-1α followed with western blot of ubiquitin or SUMO2/3 in 1% O_2 hypoxia-induced THP-1 cells. Bar graphs (**e**, **f**) present mean values ± SD, and the *p* values are calculated using a two-tailed *t*-test. * $P < 0.05$, ns $P > 0.05$. Source data are provided as a Source Data file. NES normalized enrichment scores, FDR false discovery rate, CHX cycloheximide.

signaling pathway (Fig. 3a–d), suggesting its potential importance in mediating the effects of YY1 under hypoxic conditions. Given that HIF-1α plays a fundamental role in the hypoxia signaling pathway[26,27], we used siRNA to inhibit YY1 expression and observed its impact on HIF-1α expression in THP-1 cells. Western blotting revealed a notable decrease in HIF-1α protein levels in THP-1 cells with YY1 depletion compared to that in control cells (Fig. 3e, Supplementary Fig. 2a, b), while the mRNA levels of HIF-1α remained unaffected (Fig. 3f). This finding suggested an involvement of a posttranslational mechanism that potentially stabilizes HIF-1α via YY1 in macrophages. Consistent with this hypothesis, the cycloheximide (CHX) chase assay demonstrated a significant reduction in the stability of HIF-1α upon YY1 suppression (Fig. 3g, Supplementary Fig. 2c). In addition, we observed that the proteasome inhibitor MG132 increased HIF-1α expression during hypoxia and counteracted the inhibitory effect of YY1 knockdown on HIF-1α levels (Fig. 3h, Supplementary Fig. 2d). The HIF-1α protein is known to be stabilized under hypoxic conditions and degraded through the ubiquitination-proteasome pathway in a normoxic environment[28,29]. Herein, we conducted a ubiquitin assay on the HIF-1α IP protein to assess the ubiquitination level of HIF-1α, revealing an increase in the ubiquitination level of HIF-1α following YY1 suppression (Fig. 3i, Supplementary Fig. 2e). SUMOylation has been shown to counteract the ubiquitination of substrates under specific circumstances[30,31]. Here, we found that silencing YY1 in THP-1 cells led to increased degradation of HIF-1α alongside a descending SUMOylation mediated by small ubiquitin-related modifier 2/3 (SUMO2/3)

(Fig. 3j, Supplementary Fig. 2f). Additionally, in the CHX chase assay and MG132 experiments, the suppression of SUMO2/3 using siRNAs led to an increase in HIF-1α degradation (Supplementary Fig. 2g, h). In summary, these findings confirm that YY1 promotes the stabilization of the HIF-1α protein, a process closely linked to its ubiquitination and SUMOylation.

NUSAP1 promotes HIF-1α SUMOylation and inhibits its ubiquitination

To further explore the mechanism by which YY1 stabilizes HIF-1α in macrophages, we performed MS analysis of the YY1 interactome in THP-1 cells. The results revealed NUSAP1 as a protein bound by YY1, and co-IP experiments confirmed the direct interaction between YY1 and NUSAP1 (Fig. 4a, b, Supplementary Fig. 3a). Elevated expression of NUSAP1, a microtubule-associated protein, in the TME is correlated with tumor infiltration of myeloid-derived immune cells[32]. Notably, NUSAP1 harbors an SAP domain commonly found in small ubiquitin-related modifier (SUMO) ligases that is associated with substrate recognition and ligase activity[33]. Given the role of YY1 in stabilizing HIF-1α in macrophages, we extended our investigation to ascertain whether NUSAP1 contributes to HIF-1α expression. Remarkably, silencing NUSAP1 led to substantial downregulation of HIF-1α expression (Supplementary Fig. 3b), and the MG132–CHX assay showed that NUSAP1 could bolster HIF-1α stabilization (Fig. 4c and Supplementary Fig. 3c, d). Consistent with the stabilizing effect of YY1 on HIF-1α, the ubiquitination of HIF-1α markedly increased after NUSAP1 knockdown (Fig. 4d).

Additionally, we found that knocking down NUSAP1 reduced the SUMOylation level of HIF-1α (Fig. 4e). Additionally, the use of recombinant proteins of SUMO2/3 and NUSAP1 in the purified HIF-1α protein also suggested that NUSAP1 can promote SUMO2/3-mediated SUMOylation of HIF-1α (Supplementary Fig. 3e). Furthermore, to elucidate the specific role of the SAP domain in this regulatory process, we generated a NUSAP1-ΔSAP variant lacking the SAP domain and assessed its impact on SUMOylation and HIF-1α ubiquitination (Fig. 4f). While full-length NUSAP1 promoted HIF-1α SUMOylation, the NUSAP1-ΔSAP variant failed to elicit similar effects (Fig. 4g). Notably, the full-length of NUSAP1 can restore the inhibitory effect of siYY1 on the SUMOylation of HIF-1α, whereas NUSAP1-ΔSAP cannot, indicating the involvement of NUSAP1-SAP domain in the regulation of HIF-1α SUMOylation by YY1 (Fig. 4h). These findings suggest that the interaction between YY1 and NUSAP1 facilitates the SAP domain-mediated SUMOylation of HIF-1α while inhibiting its ubiquitination, ultimately culminating in increased HIF-1α expression.

To validate the interaction between YY1 and NUSAP1, we predicted the binding sites by bioinformatics analysis, ranging mainly within amino acids 240–250 of NUSAP1 and amino acids 200–220 of YY1 (Supplementary Fig. 3f). In addition to the zinc-finger structure domain (C-terminal DNA-binding domain) mentioned above, the N-terminal domain (NTD) of YY1 has been reported to serve as the primary domain for protein modifications[34]. Here, we generated truncated forms of the N/C-terminal domains of YY1 ($YY1^{NTD}$: 1–320, $YY1^{CTD}$: 321–414) and NUSAP1 ($NUSAP1^{NTD}$: 1–158, $NUSAP1^{CTD}$: 159–441) and tagged them with EGFP or Flag, respectively (Fig. 4f and Supplementary Fig. 3g). Flag pull-down followed by co-IP assays confirmed the strong binding between YY1 and $NUSAP1^{CTD}$ (Flag-$NUSAP1^{1–158}$) but not between YY1 and $NUSAP1^{NTD}$ (Flag-$NUSAP1^{159–441}$) (Fig. 4i). Similarly, $YY1^{NTD}$ (EGFP-$YY1^{1–320}$), but not $YY1^{CTD}$ (EGFP-$YY1^{321–414}$), was found to interact with NUSAP1 (Fig. 4j). Next, we endeavored to precisely silence the regions harboring the most densely predicted sites within $YY1^{NTD}$ and $NUSAP1^{CTD}$, constructing truncated proteins tagged with Flag and HA, respectively. Our findings revealed a notable reduction in the binding between the YY1 and NUSAP1 proteins after silencing amino acids 240–250 of NUSAP1 and amino acids 200–220 of YY1. This finding suggests that the regions encompassing amino acids 240–250 of NUSAP1 and 200–220 of YY1 may represent the most crucial binding sites (Fig. 4k, l and Supplementary Fig. 3h, i). Briefly, these results obtained from the truncated proteins validated the interaction between YY1 and NUSAP1. Concurrently, given the direct involvement of the SAP domain of NUSAP1 in mediating HIF-1α SUMOylation, we further examined the interaction between NUSAP1 and HIF-1α under hypoxic conditions. To discern specific binding regions, we subdivided HIF-1α into N-terminal (HA-HIF-$1α^{1–390}$) and C-terminal (His-HIF-$1α^{391–826}$) fragments, each tagged accordingly. Through co-IP experiments, we confirmed the binding of both HIF-1α fragments to the NUSAP1 N/C-terminus (Fig. 4m, n). In summary, our investigation of the truncated proteins mentioned above elucidates the interactions involving YY1, NUSAP1, and HIF-1α.

Moreover, we examined the morphological distribution of YY1, NUSAP1, and HIF-1α in cells under normoxic/hypoxic conditions via IF imaging to further investigate the associated intracellular processes. Our findings indicate that hypoxia triggers several notable phenomena. First, YY1 significantly increased the formation of liquid separation droplets under hypoxic conditions, consistent with previous observations. Second, the distribution of NUSAP1 in cells transitioned from a uniform dispersion to punctate aggregation. Third, the expression of HIF-1α increased under hypoxia, as expected, and HIF-1α formed droplets closely associated with or even colocalized with YY1 and NUSAP1 (Fig. 4o). Surprisingly, almost the whole length of NUSAP1 was characterized as intrinsically disordered (Fig. 4p), which has been recognized as a key element in phase separation. Then, we constructed an m-cherry-tagged NUSAP1 chimeric protein and conducted IF assays to examine its ability to form condensates with different protein concentrations in solution, in which PEG 8000 and 150 mM NaCl were used to mimic the crowding situation of the intracellular environment. As expected, significant aggregation of condensates was observed with increasing NUSAP1 chimera concentration, which could be reversed by 1,6-hex (Fig. 4q). Next, we mixed YY1-IDR and non-IDR chimeras tagged with EGFP with NUSAP1-m-cherry. Strikingly, we observed obvious colocalization of NUSAP1 with YY1-IDR and full-length YY1 (Fig. 4r).

HIF-1α undergoes SUMOylation-related phase separation under hypoxic conditions

Notably, recent studies have confirmed that SUMOylation of substrates and SUMO noncovalent interactions promote SUMOylation-mediated phase separation[35,36]. To further clarify the role of phase separation in HIF-1α SUMOylation and stabilization, we generated EGFP-tagged HIF-1α chimeras based on the predicted HIF-1α IDRs, including IDR1-EGFP (EGFP-HIF-$1α^{1–80}$), IDR2-EGFP (EGFP-HIF-$1α^{391–750}$), non-IDR-EGFP (EGFP-HIF-$1α^{81–390}$), and FL-EGFP (EGFP-HIF-$1α^{full\text{-}length}$) (Fig. 5a). Fluorescence microscopic visualization of HIF-1α chimeric proteins revealed that EGFP-tagged IDR1, IDR2 and full-length protein formed significantly enlarged condensates at concentrations ranging from 5 to 10 μM, which could be further inhibited by 1,6-hex, whereas non-IDR-EGFP did not yield noticeable condensates at 10 μM (Fig. 5b, Supplementary Fig. 4a). Given that HIF-1α is highly unstable and rapidly degraded under normoxia, leading to significantly low expression levels, it is difficult to observe any visible droplets, whereas punctate aggregation can be observed under hypoxia (Fig. 4o). To clarify the phase separation characteristics of the punctate droplets we observed under hypoxia, we introduced segmented EGFP-HIF-1α plasmids into THP-1 cells and conducted live imaging using confocal fluorescence microscopy under 1% O_2 hypoxia. Under these conditions, we observed robust fluorescence expression, accompanied by the appearance of mobile condensates, confirming their liquid-like properties through fusion and fission processes (Fig. 5c, Supplementary Fig. 4b). Moreover, we conducted a fluorescence recovery after photobleaching (FRAP) assay in 1% O_2 hypoxia-preconditioned THP-1 cells. The fluorescence intensity of the HIF-1α IDRs or full-length

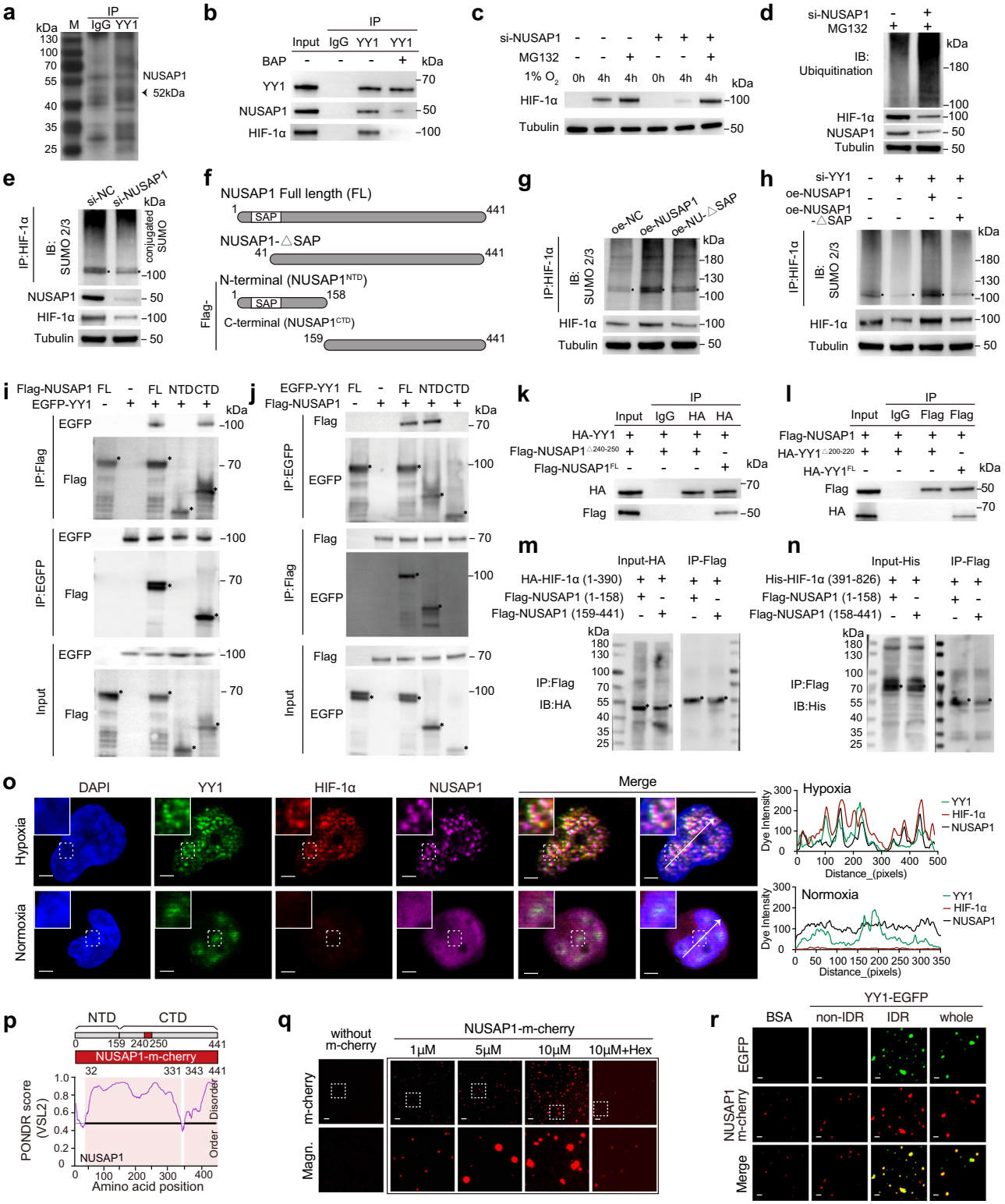

protein almost completely recovered within 80 s postbleaching, indicating that the condensed HIF-1α underwent rapid exchange with the surrounding environment in vivo (Fig. 5d, Supplementary Fig. 4c). Subsequently, the transfected THP-1 cells were fixed and stained with DAPI to observe the cellular localization of segmented HIF-1α. Non-IDR chimeras exhibited a uniform pattern in the cytoplasm and nucleus, whereas IDRs formed clustered puncta mainly in the nucleus (Fig. 5e). Furthermore, deletion of the IDR1 or IDR2 domains from the HIF-1α full-length plasmid suppressed phase-separated droplet formation. Notably, deletion of IDR1 resulted in predominant nuclear localization of the protein, whereas deletion of IDR2 led to an even distribution throughout the cells (Fig. 5f), suggesting that the IDR2 domain may facilitate the nuclear entry of HIF-1α under hypoxic conditions.

Next, we used subasumstat (TAK-981), a small molecule SUMOylation inhibitor, to determine the effect of SUMOylation on the formation of HIF-1α phase-separated droplets. Immunofluorescence

Fig. 4 | YY1 promotes the stability of HIF-1α by binding to NUSAP1. a Mass spectrometry of proteins immunoprecipitated with YY1 and IgG under $CoCl_2$ treatment conditions. **b** In the co-IP experiment using 1% O_2 hypoxia-induced THP-1 cells, the expression levels of YY1, NUSAP1, and HIF-1α proteins were detected in the proteins immunoprecipitated by the YY1 or IgG antibody. **c** Western blot of HIF-1α in THP-1 cells treated with MG132. **d**, **e** Western blot of ubiquitin or SUMO2/3 following HIF-1α IP in hypoxia-induced THP-1 cells. **f** Diagram of the SAP domain and N/C-terminus of NUSAP1. **g**, **h** SUMOylation assays in hypoxia-induced THP-1 cells under the indicated conditions. **i** CO-IP assays in hypoxia-induced THP-1 cells showing the interactions between Flag-tagged NUSAP1 segments and EGFP-tagged YY1. **j** CO-IP assays in hypoxia-induced THP-1 cells showing the interactions between EGFP-tagged YY1 segments and Flag-tagged NUSAP1. FL, NTD, and CTD represent the full-length, N-terminal domain, and C-terminal domain of YY1, respectively. **k**, **l** Co-IP assays showing the interactions of the indicated HA-YY1 or Flag-NUSAP1 mutant. **m**, **n** Co-IP assays showing the interactions of truncated HIF-1α and NUSAP1 proteins in hypoxia-induced THP-1 cells. **o** Immunofluorescence assays showing the colocalization of the indicated markers in THP-1 cells treated with hypoxia or normoxia. The dye intensity alongside the white lines was calculated and plotted in the right panels. Scale bar, 2 μm. **p** Schematic diagram of the NUSAP1 IDR. **q** Fluorescence images of m-cherry showing droplet formation in the medium under different concentrations of NUSAP1-m-cherry protein. Scale bar, 5 μm. **r** Fluorescence images of EGFP and m-cherry showing the physical colocalization of NUSAP1-m-cherry with the YY1-IDR-EGFP or YY1-non-IDR-EGFP in the medium. Scale bar, 5 μm. Source data are provided as a Source Data file. NTD N-terminal domain, CTD C-terminal domain, FL full-length.

analysis of HIF-1α revealed that TAK-981 significantly reduced the density and fluorescence intensity of hypoxia-induced endogenous HIF-1α phase separation droplets in THP-1 cells (Fig. 5g). In addition, we predicted and scored the SUMOylation sites of HIF-1α with the SUMOplot Analysis Program and focused on the top two sites (amino acids 477 and 391) with scores >0.9 (Fig. 5h). We constructed HIF-1α full-length plasmids containing EGFP and the K477F and K391F mutants. The SUMOylation of K391F-mutated HIF-1α decreased in expression under hypoxia compared with that of the full-length protein (Fig. 5i, Supplementary Fig. 4d). Additionally, although the K477F mutation led to a lack of large condensates, we still observed abundant droplets in most cells (Fig. 5j). However, in the K391F mutant group, only a relatively diffuse pattern of EGFP fluorescence was observed. These results show that hypoxia induces the HIF-1α protein to aggregate in the nucleus and form punctate phase-separation droplets regulated by SUMOylation.

Targeting the YY1–NUSAP1–HIF-1α nexus in macrophages inhibits PCa tumor growth in vivo

To explore the therapeutic effects of targeting the YY1–NUSAP1–HIF-1α nexus in macrophages, we employed Discovery Studio software to dock 1729 small molecules against these three proteins. Among them, tenapanor (T7587, CAS #1234423-95-0), a sodium/hydrogen exchanger 3 inhibitor currently used to treat hyperphosphatemia in long-term dialysis patients[37], emerged with a top 10 docking score across all three proteins. Additionally, we utilized web servers AlphaFold, HDOCK, and Rosetta to generate protein–protein interaction, analyzing amino acid properties and atomic spatial information to pinpoint interaction sites. Comparing the spatial positions of protein interaction sites with those of small molecules revealed a spatial clash between tenapanor's predicted protein–protein interaction domain and the YY1–NUSAP1–HIF-1α interaction domains (Supplementary Fig. 5a). Specially, we also predicted that tenapanor spatially clashes to the key binding domains ($YY1^{200\text{-}220}$ and $NUSAP1^{240\text{-}250}$) we verified (Fig. 6a and Supplementary Fig. 5b), and confirmed the interaction between tenapanor with $YY1^{NTD}$ and $NUSAP1^{CTD}$ by using the biotin-labeled tenapanor (Supplementary Fig. 5c), suggesting that tenapanor may competitively inhibit YY1–NUSAP1 interaction. To validate the role of tenapanor in the YY1–NUSAP1–HIF-1α nexus, we conducted an IP analysis in THP-1 cells treated with either tenapanor or DMSO. The results confirmed that tenapanor significantly suppressed the binding of YY1 and HIF-1α to NUSAP1 (Fig. 6b, c).

To verify the effect of tenapanor in vivo, we used RM-1 cells to construct subcutaneous tumor-bearing mice (Fig. 6d). To better target TAMs in the TME, a reported TAM-targeting peptide (M2pep) synthesized on a liposome carrier[38] was introduced to load tenapanor or the control solvent (TEN-M2pep/NC-M2pep). To clarify its distribution in mouse tissues, we constructed a fluorescent label on TEN-M2pep. Tracer imaging technology further confirmed a noticeable enrichment of TEN-M2pep in mouse subcutaneous tumors within the first 2 days after injection (Supplementary Fig. 5d). Notably, during the 1-month observation period after the injection, the growth curve showed that compared with the control treatment, TEN-M2pep significantly hampered tumor growth in the mice (Fig. 6e). Additionally, we performed RNA sequencing on isolated CD45-positive cells from the harvested tumor suspensions, revealing significant enrichment of pathways related to T-cell proliferation and activation in the TEN-M2pep-treated group (Fig. 6f, g, Supplementary Fig. 5e). Meanwhile, we also observed an increased proportion of tumor-infiltrated $CD8^+$ T cells in the TEN-M2pep group by immunohistochemistry and flow cytometry (FC) analyses (Fig. 6h, i).

The efficacy of immune checkpoint inhibitors in tumors largely depends on the quantity of effector T cells in the TME. Herein, we investigated the effect of combination treatment with TEN-M2pep and a PD-1 inhibitor in a PCa subcutaneous allograft mouse model. The results showed that the PD-1 inhibitor had a limited tumor suppressive effect on the subcutaneous tumor model, whereas the tumors grew significantly more slowly after the combination of the PD-1 inhibitor with TEN-M2pep (Fig. 6e). Next, we used OVA-RM-1 cells expressing ovalbumin (OVA) as a neotumor antigen to construct a mouse subcutaneous PCa tumor model. T cells sorted from OT-1 mouse spleens (OT-1 T cells) were injected into OVA-RM-1 tumor-bearing mice to generate tumor-specific exogenous T cells. We found that the combination of OT-1 T cells and TEN-M2pep significantly reduced subcutaneous tumor growth compared to OT-1 T cells alone. Moreover, in the presence of tumor-specific exogenous T cells, the combination of TEN-M2pep and the PD-1 inhibitor exhibits superior subcutaneous tumor inhibition compared to either treatment alone (Fig. 6e, Supplementary Fig. 5f). Notably, neither TEN-M2pep nor the PD-1 inhibitor caused significant morphological changes in the mice's supportive organs or body weight, preliminarily indicating the safety of tenapanor in vivo (Supplementary Fig. 5g). FC analysis of subcutaneous tumors revealed that TEN-M2pep increased the proportion of endogenous $CD8^+$ T cells in tumors but had a limited effect on exogenous $CD8^+$ T cells from OT-1-treated mice (Supplementary Fig. 5h–j).

Construction and application of YY1-DbTACs and YY1-DcTACs in an allogeneic mouse transplantation model

Considering the critical role of YY1, we further investigated strategies for impeding the progression of PCa by degrading the YY1 protein. Currently, due to challenges in developing YY1 into a therapeutic agent, there is still a lack of YY1-targeted drugs for clinical use[39]. Proteolytic targeting chimeras (PROTACs) are bifunctional small molecules that can simultaneously bind target proteins and E3 ubiquitin ligases and are a promising strategy for degrading target proteins through the ubiquitin–proteasome system[40]. Hence, we innovatively designed and constructed YY1-targeted DNA-based PROTACs (YY1-DbTACs) to degrade the YY1 protein (Fig. 7a). This process involved coupling a dibenzo-cyclooctyne (DBCO)-modified DNA strand S1 with an azide-modified E3 ligase ligand through click chemistry. The 5′ end of the DNA strand S2 extended the YY1 binding sequence as the target protein ligand. The above two complementary paired DNA strands

https://doi.org/10.1038/s41467-025-61560-0

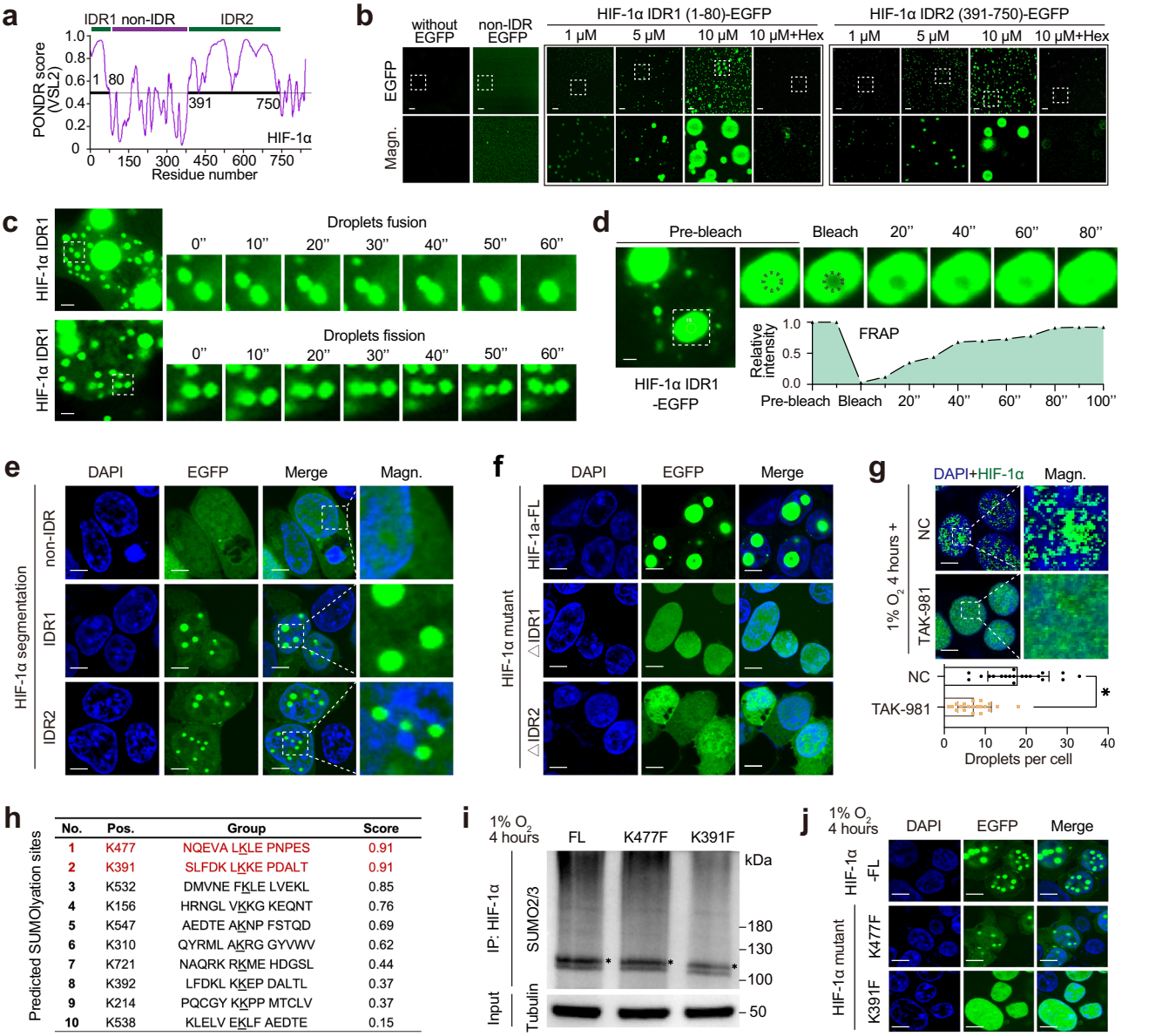

Fig. 5 | HIF-1α undergoes SUMOylation-related phase separation under hypoxia. a Diagram showing the intrinsically disordered protein regions (IDRs) of HIF-1α. **b** Representative images of phase separation condensates based on HIF-1α-IDR1/2-EGFP with different protein concentrations or with 1,6-hexanediol. Scale bar, 5 μm. **c** The process of fusion and fission in HIF-1α-IDR1-EGFP-mediated condensates. Scale bar, 1 μm. **d** Fluorescence intensity of the condensate during fluorescence recovery after photobleaching (FRAP) assay. Scale bar, 1 μm. The average relative fluorescence intensities are plotted as white circles. **e** Localization of HIF-1α-IDRs-EGFP and HIF-1α-non-IDR-EGFP in THP-1 cells after 4 h of 1% O_2 hypoxia and fixation. Scale bar, 5 μm. **f** Representative fluorescence images of EGFP and DAPI showing the patterns of HIF-1α mutants. Scale bar, 5 μm. **g** Immunofluorescence staining of HIF-1α in THP-1 cells treated with TAK-981 or control solution under 1% O_2 hypoxia. Twenty cells randomly selected from three repeated groups were analyzed. Scale bar, 5 μm. The bar graph in the lower panel presents mean values ± SD, and the *p* values are calculated using a two-tailed *t*-test ($P < 0.001$). *$P < 0.05$. **h** The predicted SUMOylation sites in HIF-1α based on the SUMOplot Analysis Program. **i**, **j** SUMO2/3-mediated SUMOylation and immunofluorescence staining in 1% O_2 hypoxia-induced THP-1 cells with the HIF-1α K477F or K391F mutation. Scale bar, 5 μm. Source data are provided as a Source Data file. IDR intrinsically disordered regions, FL full-length.

self-assembled into YY1-targeted DNA-based PROTACs (YY1-DbTACs) through thermal annealing. The covalent attachment of ligands and the self-assembly of YY1-DbTACs were confirmed by polyacrylamide gel electrophoresis (PAGE) (Supplementary Fig. 6a). To investigate the degradation kinetics of YY1-DbTACs in vitro, we incubated THP-1 cells with YY1-DbTACs at various concentrations and for various durations. Western blotting confirmed that YY1-DbTACs exhibited concentration- and time-dependent degradation of the YY1 protein (Fig. 7b). The slight recovery after 36 h may result from counteracting factors, such as the degradation of the DNA double-stranded structure of YY1-DbTACs within 24 h, while YY1 continues to be synthesized. In addition, the degradation mechanism suggested that YY1-DbTACs enhanced YY1 ubiquitination and degradation (Fig. 7c). As expected, YY1-DbTACs effectively degraded the YY1 protein through the ubiquitination pathway.

To investigate the fate of YY1-DbTACs in vivo, we injected jetPEI reagent-transfected Cy7-labeled YY1-DbTACs (Cy7-YY1-DbTACs@jetPEI) and free Cy7 dye into the tail veins of allogeneic transplanted mice. Fluorescent images of the mice were collected at different time points after the injection through small animal in vivo imaging. The fluorescence intensity at the tumor site of mice injected with Cy7-YY1-DbTACs@jetPEI significantly increased during the experimental period. The tumor site of mice injected with Cy7 peaked at 2 h and then continuously decreased (Supplementary Fig. 6b). The fluorescence

https://doi.org/10.1038/s41467-025-61560-0

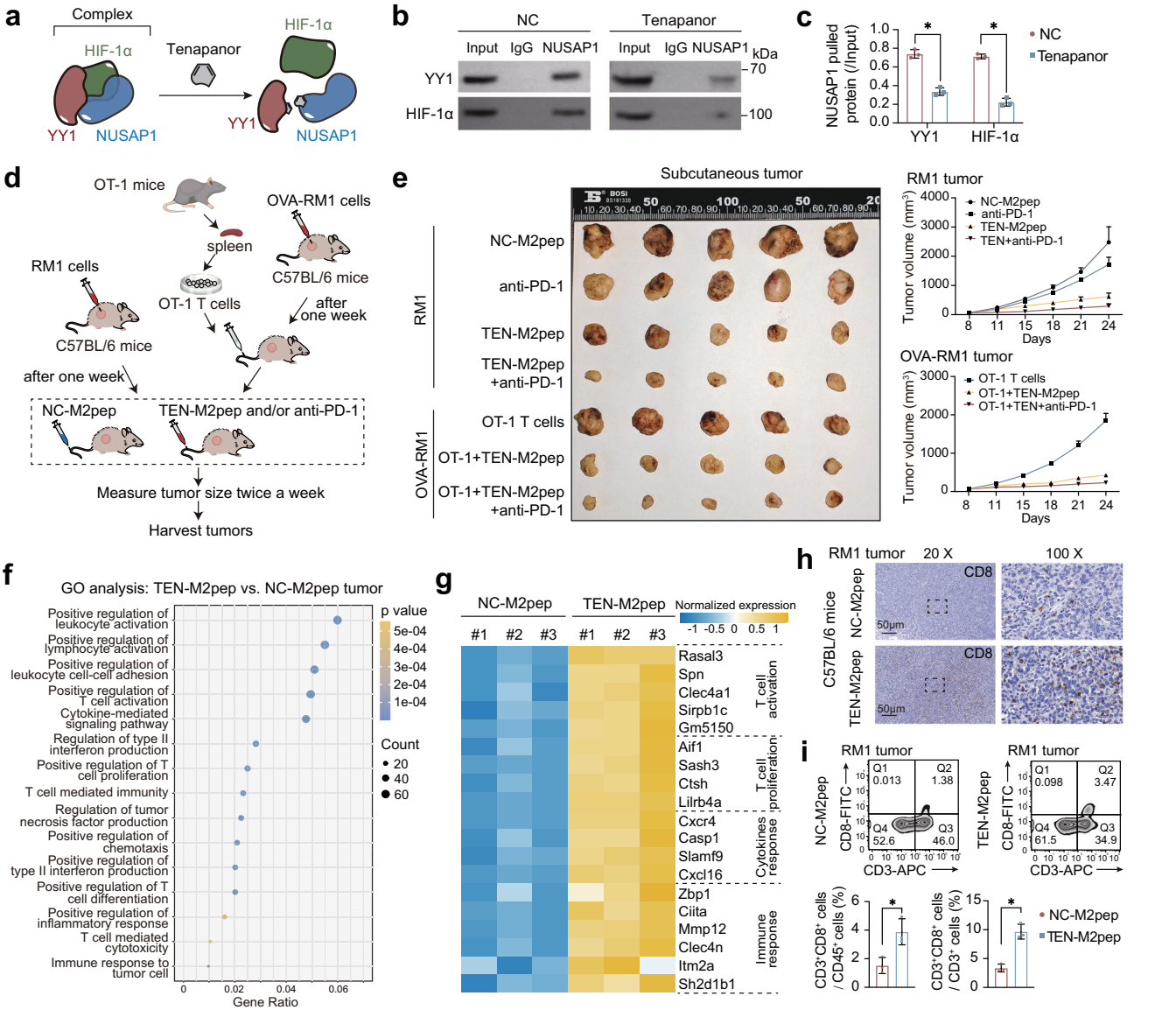

Fig. 6 | A small molecule inhibitor targeting the YY1–NUSAP1–HIF-1α interaction suppressed PCa progression. a Schematic diagram showing that tenapanor inhibits the binding of the YY1–NUSAP1–HIF-1α nexus. **b**, **c** Co-IP of NUSAP1 showed that its interactions with YY1 and HIF-1α were suppressed by tenapanor. The protein intensity of YY1 and HIF-1α pulled down from NUSAP1 was analyzed with ImageJ and standardized to that of the input samples from the same experiment. The blots were processed in parallel ($n = 3$ independent experiments, $P < 0.001$ and $P < 0.001$). *$P < 0.05$. **d**, **e** Schematic diagram and tumor growth curve of the effects of TEN-M2pep and control medium on subcutaneous tumorigenesis in mice. Each experimental group consisted of five male C57BL/6 mice, all aged 6–8 weeks. The right panels present the mean values ± SD at each time point ($n = 5$ independent experiments, one-way ANOVA followed by Tukey test based on data in the last time point). **f**, **g** GO analysis based on RNA-sequencing data of CD45-sorted cells from TEN-M2pep-treated subcutaneous tumors showing enriched immune response-related pathways and representative upregulated genes (two-tailed *t*-test). **h**, **i** Immunohistochemical staining and flow cytometry of subcutaneous tumors showing the infiltration of $CD8^+$ T cells in the indicated groups ($n = 3$ independent experiments, $P = 0.019$ and $P = 0.002$). Bar graphs (**c**, **i**) present the mean values ± SD, and the *p* values are calculated using a two-tailed *t*-test. * $P < 0.05$. Source data are provided as a Source Data file.

intensity analysis of isolated mouse organs and tumor tissues revealed that compared with Cy7, Cy7-YY1-DbTACs@jetpei was enriched in tumor tissues after 48 h and was metabolized by the liver and kidney (Supplementary Fig. 6c).

The primary reason for the difference in metabolism between the two treatment groups may be the strong lipophilicity of the jetPEI carrier. These results suggest that YY1-DbTACs@jetPEI can accumulate in tumors and exhibit targeting ability. To target YY1 in tumor macrophages, M2pep was combined with YY1-DbTACs@jetPEI. RM-1 cells were used to establish a subcutaneous PCa tumor model in mice, and the distribution and role of M2pep-YY1-DbTACs@jetPEI in subcutaneous tumors were observed via tail vein injection (Fig. 7d). Fluorescence detection in mice showed that supplementation with M2pep did not significantly inhibit the enrichment of YY1-DbTACs in subcutaneous tumor tissues (Supplementary Fig. 6d). After the intermittent tail vein injection of M2pep-YY1/NC-DbTACs@jetPEI for 3 weeks, the growth of subcutaneous tumors in the M2pep-YY1-DbTACs@jetPEI group was significantly suppressed (Fig. 7e).

Despite the development of M2pep-YY1-DbTACs@jetPEI capable of targeting and degrading YY1, the double-stranded DNA structure of YY1-DbTACs is rapidly degraded within 24 h by nucleases in cells, resulting in a higher dosing frequency, lower applicability, and significant challenges in clinical application due to the difficult and costly preparation of M2pep-loaded liposomes. Therefore, based on a previously reported covalent DNA framework-based PROTACs system[41], YY1-targeted tetrahedral DNA-caged PROTACs (YY1-DcTACs) were

https://doi.org/10.1038/s41467-025-61560-0

designed and constructed to achieve prolonged degradation of the YY1 protein in M2 macrophages (Fig. 7f). This tetrahedral DNA nanostructure (YY1-DcTACs) contains a macrophage marker CD206 mRNA response switch to release YY1-DbTACs in M2 macrophages.

Specifically, an azide-modified E3 ligand is coupled to the DBCO-modified nucleotide site inside the tetrahedron, while the other side of the reported DNA tetrahedral framework is replaced by the binding sequence of YY1 as the target protein ligand. The cage structure of the tetrahedron insulates the E3 ubiquitin ligand to prevent its binding to the E3 ubiquitin ligase, thus blocking YY1-DbTACs. The complementary DNA (cDNA) strand S1 of the modified nucleic acid site was designed as an antisense sequence against CD206 mRNA. Triggered by CD206 mRNA in TAMs, DNA strand S1 dissociates, opening the cage-like structure of the tetrahedron and releasing YY1-DbTACs. The formation of the intact tetrahedron was confirmed by PAGE analysis (Supplementary Fig. 6e). To further test the stability of DcTACs under physiological conditions, YY1-DcTACs were incubated in 10% FBS-containing medium for 24 h, and the results showed that YY1-DcTACs

Fig. 7 | Construction and application of YY1-DbTACs@jetPEI and transgenic mice. a Schematic diagram illustrating the mechanism of YY1-DbTACs-mediated degradation of YY1. **b** Western blot in THP-1 cells treated with YY1-DbTACs. **c** Western blot of ubiquitin following HIF-1α IP in hypoxia-induced THP-1 cells treated with YY1-DbTACs. **d** Experimental flow chart of subcutaneous tumorigenesis in mice using M2pep-YY1/NC-DbTACs@jetPEI. Each experimental group consisted of five male C57BL/6 mice (6–8 weeks). **e** Tumor volume changes over 21 days following subcutaneous tumor implantation. The lower panel presents the mean values ± SD at each time point. The *p* values were calculated based on the last time point between two datasets using a two-tailed *t*-test ($n = 5$ independent experiments, $P < 0.001$). *$P < 0.05$. **f** Schematic diagram illustrating the mechanism of YY1-DcTACs and its tetrahedral structure. **g** Confocal microscopy images showing the responsiveness of YY1-DcTACs-FAM/BHQ1 in the indicated cell lines. **h** Changes in tumor volume within 14 days after injection of YY1/NC-DcTACs via the tail vein in a mouse subcutaneous tumor model. The T lymphocytes were sorted by flow cytometry before testing changes in the ratio of $CD3^+CD8^+$ T cells. The lower panel presents the mean values ± SD at each time point. The *p* values were calculated based on the last time point between the two datasets (two-tailed *t*-test, $P < 0.001$). *$P < 0.05$. **i** Schematic diagram illustrating the construction of YY1 transgenic mice with myeloid conditional knockout and the establishment of a subcutaneous tumorigenesis model. **j** Subcutaneous tumor size in mice after 21 days of tumor formation ($n = 5$ independent experiments, $P < 0.001$). Five wild-type male C57BL/6J mice and five C57BL/6J-$YY1^{em1Cflox}$ male mice were used in the experiment (6–8 weeks old). **k** T lymphocytes were sorted by flow cytometry in the CD45-gated immune cells after grinding the subcutaneous tumors of transgenic mice into a cell suspension, and changes in the ratio of $CD3^+CD8^+$ T cells were observed ($n = 5$ independent experiments, $P < 0.001$). Bar graphs (**h**, **j**, **k**) present the mean values ± SD, and the *p* values are calculated using a two-tailed *t*-test. * $P < 0.05$. Source data are provided as a Source Data file.

did not degrade significantly (Supplementary Fig. 6f). To investigate the response efficiency of YY1-DcTACs to CD206, we introduced CD206 mRNA into YY1-DcTACs for strand displacement. The free energy required for the self-assembly (I) and responsive strand displacement (II) of YY1-DcTACs was calculated. The Δ G value between them indicated that YY1-DcTACs could spontaneously respond to CD206 mRNA and undergo strand displacement. Notably, the PAGE results confirmed that S1 and CD206 mRNA were bound at a 1:1 ratio, while the YY1-DcTACs completely dissociated (Supplementary Fig. 6g). To further investigate the response efficiency of YY1-DcTACs in living cells, a pair of base pairs on the S1 chain and its complementary chain were modified with FAM fluorophores and BHQ1 quenched groups, respectively, and these DNA strands self-assembled to form modified YY1-DcTACs (YY1-DcTACs-FAM/BHQ1). The fluorescence of YY1-DcTACs-FAM/BHQ1 was quenched due to the close spatial distance between BHQ1 and FAM (<3 nm). In TAMs, the S1 sequence modified with BHQ1 dissociated upon complementarity with CD206 mRNA, and the fluorescence of YY1-DcTACs-FAM/BHQ1 was restored (Supplementary Fig. 6h). The fluorescence pattern confirmed that the fluorescence intensity of YY1-DcTACs-FAM/BHQ1 recovered significantly after the addition of CD206 mRNA (Supplementary Fig. 6i). Confocal images revealed that YY1-DcTACs-FAM/BHQ1 responded only to M2 macrophages and not to normal L02 cells, RM-1 cells, M0 macrophages, and M1 macrophages (Fig. 7g). To further investigate the response efficiency of YY1-DcTACs in vivo, the FAM/BHQ1 fluorophore/quencher pairs were substituted with CY5/BHQ3 fluorophore/quencher pairs (ResDcTACs-CY5/BHQ3). ResDcTACs-CY5/BHQ3, YY1-DcTACs labeled with CY5 (DcTACs-CY5), and nonresponsive YY1-DcTACs labeled with the CY5/BHQ2 pair (nonResDcTACs-CY5/BHQ3) were injected into the tail veins of allogeneic transplanted mice. Immunofluorescence colocalization analysis demonstrated that YY1-DcTACs strongly colocalized with CD206 at the tumor site (Supplementary Fig. 6j). These results indicate that YY1-DcTACs can specifically induce the release of YY1-DbTACs in tumor tissues through CD206 mRNA. The fluorescence imaging results demonstrated that the fluorescence intensity at the tumor site in the mice injected with DbTACs-CY5 peaked at 3 h and then continuously decreased slowly (Supplementary Fig. 6k). Using a similar subcutaneous tumorigenesis model and NC/YY1-DcTACs tail vein injection treatment described above, we observed a remarkable tumor inhibitory effect of YY1-DcTACs until the 14th day (Fig. 7h). The subsequent single-cell sequencing on subcutaneous tumors revealed the activation of immune response pathways in the YY1-DcTACs group. The cell subset analysis indicated an increase in the proportion of T cells, with a rise in $CD8^+$ effector memory T cells (Tem) and a decrease in $CD8^+$ exhausted T cells (Tex) within the YY1-DcTACs group (Supplementary Fig. 7a–d), which were confirmed by flow cytometric analysis (Supplementary Fig. 7e–j). Next, FITC/BHQ1 fluorophore-quencher pairs were site-specifically conjugated to YY1-DcTACs via a protocol analogous to the aforementioned methodology to validate the specific function of YY1-DcTACs in M2 macrophages. Following 12 h of systemic administration, tumor tissues were dissociated to generate single-cell suspensions, which were subsequently subjected to FC analysis with a panel of markers, including CD45, CD11b, F4/80, and either CD206 (M2 marker) or CD86 (M1 marker). The results revealed preferential enrichment of the YY1-DcTAC labels within the $CD206^+$ macrophage subpopulation, whereas minimal function was detected in $CD86^+$ macrophages. (Supplementary Fig. 8a, b). Furthermore, the multiplex IF analysis of tumor tissue also revealed the significantly reduced YY1 expression in $CD206^+$ cells in the YY1-DcTACs group compared to the NC-DcTACs group (Supplementary Fig. 8c).

To further assess the influence of macrophage YY1 on subcutaneous tumor development, we engineered conditional knockout C57BL/6J-$YY1^{em1Cflox}$ mice with YY1 specifically depleted in macrophages (Fig. 7i). Through the genetic characterization of bone marrow-derived macrophages (BMDMs) and cells obtained from mouse tails, we clearly delineated the marked suppression of YY1 expression in macrophages compared to that in somatic cells (Supplementary Fig. 8d). Subsequent subcutaneous tumor experiments conducted on C57BL/6J-$YY1^{em1Cflox}$ and wild-type mice revealed a noteworthy inhibition of tumor growth in the transgenic mice (Fig. 7j). FC analysis revealed that conditional knockout of YY1 markedly elevated the ratio of $CD3^+CD8^+$ cytotoxic T cells to CD45-labeled T cells within subcutaneous tumors (Fig. 7k, Supplementary Fig. 8e).

In conclusion, we confirmed that suppressing YY1 levels in macrophages effectively restrains PCa growth in vivo through the conditional knockout of the YY1 gene or targeted YY1 protein degradation. Notably, tetrahedral nanostructures employing PROTAC technology may pave the way for material advancements toward clinical applications targeting YY1.

Discussion

YY1, a highly evolutionarily conserved nuclear transcription factor, exerts regulatory control over ~7% of human genes[42]. The significance of YY1 extends to various facets of tumor progression, including cell proliferation, DNA repair, epigenetic modification, and tumor immune regulation[43–45]. Our previous study revealed notable expression of YY1 in macrophages and a significant association between increased YY1 expression in TAMs and poorer prognosis in PCa patients[46]. In the present study, we initially observed an elevated ratio of $YY1^+$ macrophages within hypoxic regions, and we further elucidated the role of YY1 in promoting the infiltration of macrophages into hypoxic areas and stabilizing the HIF-1α protein. Therapeutic interventions targeting macrophage YY1, along with the use of a transgenic mouse model with conditional knockout of YY1 in macrophages, demonstrated remarkable efficacy in subcutaneous tumor-bearing mouse models. These findings unveil promising avenues for clinical strategies for PCa treatment.

Phase separation is a mechanism that explains the process of multivariate mixtures aggregating into subcellular structures to regionalize synergistically acting molecules, thus accelerating downstream transcription[47]. The occurrence of phase separation typically hinges on the presence of IDRs and protein oligomerization binding regions within the amino acid sequence of a protein[48]. In this study, we also discovered that YY1, NUSAP1, and HIF-1α possess IDR domains, rendering them capable of undergoing phase separation. These three proteins can colocalize and form phase-separated droplets within the cell nucleus, especially under hypoxic conditions. Knocking out the functional fragments within the IDR region markedly diminished the occurrence of phase separation. These findings suggest that the phase separation mechanism plays a crucial role in the YY1-mediated stabilization of HIF-1α. Additionally, the formation and stability of phase separation are regulated by various factors, including protein post-translational modifications (PTMs)[49]. Herein, we discovered that phosphorylation of YY1 and SUMOylation of HIF-1α enhance their phase separation. Moreover, mutations at relevant protein modification sites reduced the formation of phase-separated droplets, directly impacting protein function. It has been reported that PTMs, such as phosphorylation, ubiquitination, and SUMOylation, can modify the charge properties of amino acid residues, alter local structures, and facilitate intermolecular charge interactions, thereby regulating the intracellular formation of phase separation[50,51]. Our study highlights the crucial role of PTM in the mechanism of phase separation in YY1 and HIF-1α.

In our quest to identify the kinases responsible for YY1 tyrosine phosphorylation, we searched for tyrosine kinases in both the YY1 IP-MS results and a reported RNA-seq dataset from hypoxia-induced macrophages (GSE16099), ultimately pinpointing Lyn as a key candidate. Subsequent experiments under hypoxic and normoxic conditions, including IP and IF assays, confirmed that hypoxia enhances the interaction between YY1 and Lyn, and that Lyn inhibition reduces the formation of YY1 droplets under hypoxia. However, we also observed that there were other candidates in the aforementioned datasets, including EGFR in the YY1 IP-MS results and Met, Src, Itk, and Tyk2 in the hypoxia-induced macrophages. Meanwhile, we recognize that other kinases, including Src and CK2α, have been previously reported in the regulation of YY1 phosphorylation[52,53], and some of them are also present in our results. Although we have focused on Lyn due to its consistent upregulation across multiple distinct datasets and its experimentally validated role, we acknowledge that other kinases may contribute to YY1 phosphorylation in different contexts, particularly in the context of tumors.

Hypoxia and overexpression of HIF-1α are involved in tumor initiation and progression, and immune escape[7]. The ubiquitin–proteasome system is the classical pathway involved in the stabilization of HIF-1α[54]. Under normoxic conditions, HIF-1α undergoes hydroxylation by prolyl hydroxylases, leading to its recognition by the von Hippel–Lindau E3 ligase (VHL), ubiquitination, and subsequent proteasomal degradation. VHL orchestrates the swift degradation of HIF-1α under normoxia. Conversely, in hypoxic environments, the oxygen-independent slow degradation of HIF-1α further modulates its stability[55]. As a PTM akin to ubiquitination, SUMOylation affects the ubiquitination process and subsequent substrate degradation[56]. SUMOylation modifications can potentially occupy protein ubiquitination sites, thereby reducing protein ubiquitination levels and stabilizing proteins. Studies have revealed that RSUME[57] and Cbx4[58] can enhance HIF-1α SUMOylation, promoting its stability and transcriptional activity under hypoxia. In this study, we report for the first time that NUSAP1 can also modify the HIF-1α protein through its SUMOylation, thus inhibiting HIF-1α ubiquitination and increasing its stability. NUSAP1, a microtubule-associated protein related to mitosis, is implicated in various biological processes, including tumorigenesis[59]. Notably, NUSAP1 contains an SAP domain, which is known to be pivotal for regulating SUMO ligase activity[31]. The SUMOylation sites of HIF-1α are rare, with only a few studies indicating that the C-terminus of HIF-1α, particularly residues K391 and K477, may serve as the primary cluster of SUMOylation sites; previous studies have indicated that mutations at both sites can diminish HIF-1α expression within the nucleus and its transcriptional activity[58,60,61]. However, research delineating the disparity between these two sites remains scarce. Interestingly, we discovered that K391 might exert a more significant effect than K477 on inducing HIF-1α SUMOylation-mediated phase separation.

Due to the structural heterogeneity of YY1 and the lack of active sites, few YY1 inhibitors have been applied for clinical tumor treatment[39]. PROTACs are heterodifunctional molecules that utilize the cell's ubiquitin–proteasome system to degrade targeted proteins of interest, enabling the degradation of "undruggable" proteins[40,62]. In this study, we introduced a cage-like tetrahedral nucleic acid structure, YY1-DcTACs, based on the PROTAC technique, which can selectively release DNA-based PROTACs (YY1-DbTACs), effectively degrading the YY1 protein in macrophages and demonstrating its antitumor effects. Furthermore, we have shown that YY1-DcTACs exhibit significant advantages over YY1-DbTACs in terms of structural design and functional characteristics. Specifically, the unique rigid tetrahedral structure of YY1-DcTACs endows them with a longer drug residence time than YY1-DbTACs, thus significantly enhancing therapeutic efficacy. Additionally, the specific response mechanism of YY1-DcTACs, which specifically degrades the YY1 protein in macrophages, provides high precision. These unique properties exhibit tremendous potential in clinical applications, enabling therapeutic effects at lower effective doses while extending treatment intervals and reducing treatment frequency and potential side effects. However, the drug loading capacity of YY1-DcTACs is relatively limited, with each DcTAC molecule effectively releasing only one DbTAC molecule, which limits its therapeutic potential to some extent. Overall, YY1-DcTACs present prospects for targeting "undruggable" YY1 in clinical therapy for PCa, offering innovative treatment approaches. We anticipate that integrating PROTACs with nanonucleic acids will yield promising solutions for future clinical tumor treatment.

In conclusion, we observed that $YY1^{+}$ macrophages infiltrate the hypoxic regions of PCa cells. Hypoxia triggers YY1 phosphorylation in macrophages, inducing its phase separation. Concurrently, YY1 interacts with NUSAP1 and promotes the SUMOylation of HIF-1α, inhibiting its ubiquitination and thus stabilizing HIF-1α expression. In vivo experiments confirmed that therapy targeting YY1 or the combination of YY1–NUSAP1–HIF-1α inhibits subcutaneous tumor growth in mice. Our study provides insights into the mechanisms of YY1 and HIF-1α in TAMs and provides a solid theoretical basis for the advancement of PCa treatment.

Methods

Human tissue samples and tissue microarray

Paraffin-embedded PCa tissue samples were collected from patients who underwent radical prostatectomy between August 2019 and August 2023 in Southeast University Zhongda Hospital. Patients with distant metastasis or receiving androgen deprivation therapy, immune therapy, radiotherapy, or chemotherapy were excluded. At least two pathologists confirmed the pathological diagnosis. A tissue microarray was constructed using 47 tissue cores (PCa tissue) obtained from tumor centers of different PCa tissues and 30 normal gland tissue cores (Para-cancerous tissue) adjacent to cancerous regions. Each core had a diameter of 1 mm. One core from the PCa tissue and four cores from the Para-cancerous tissue were excluded due to the tissue area being less than 50% of the designated area. The baseline information of included patients was listed in Supplementary Table 1. The collection and use of clinical samples are completed under the supervision of Ethics Committee of Zhongda Hospital, Southeast University

(approval ID 2022ZDKYSB099), and written informed consent was obtained from all recruited volunteers in accordance with the committee's guidelines. Volunteers received financial compensation for travel and examination costs incurred due to additional follow-up visits.

Imaging mass cytometry (IMC)

After slicing the tissue microarray continuously, one slice was chosen for hematoxylin and eosin staining. The histological type of each core was verified by two pathologists. Following this, the labeled sections were stained with IMC target antibodies containing metal labels. These pre-sections were then scanned using the Hyperion Imaging System (Fluidigm) to generate multiplexed images. Subsequently, the acquired data underwent analysis through several steps[63]: spillover signal compensation was performed using a predefined spillover matrix to correct for signal overlap between metal channels. Next, image denoising was achieved via median filtering with a 3 × 3 window to suppress noise while preserving image features. Image contrast was then enhanced using the MATLAB function "imadjust" to improve the distribution of intensity values. Finally, cell segmentation was conducted using a connectivity-aware method with the MATLAB function "regionprops" to detect connected components and identify individual cells, with artifacts removed based on their distance to nuclei centroids. Furthermore, to identify the local accumulation of a specific cell type and its neighboring cells, the patch and milieu detection algorithm[64] was employed to investigate the correlation among YY1, CD68, and HIF-1α. To be precise, patches were defined as clusters containing at least 10 cells, with a maximum intercellular distance of 15 μm. Adjacent regions meeting these criteria were merged to form larger patches for downstream analysis. The expression levels of the markers were normalized using the *z*-score method, and a threshold value of 0.5 was applied to distinguish between positive and negative expression.

Cell lines and culture

Human monocyte THP-1 and mouse macrophage RAW264.7 cell lines were provided by the American Type Culture Collection (ATCC, USA). Cells were incubated in the RPMI 1640 medium (Gibco, Thermo Fisher Scientific, USA, cat. 11875093) or DMEM medium (Gibco, cat. 12491015) containing 10% fetal bovine serum (FBS, Gibco), 1% penicillin G and streptomycin sodium (Gibco, cat. 15070063). For normal conditions, cells were cultured at 37 °C with 5% CO_2 in a humidified incubator. For chemical hypoxic conditions, cells were cultured at 37 °C with 5% CO_2, adding cobalt chloride ($CoCl_2$) into the medium. For reoxygenation, the medium containing $CoCl_2$ was removed after 8 h, and the cells were gently washed twice with PBS to remove residual $CoCl_2$. The cells were then placed back into normal culture conditions (37 °C, 5% CO_2) for reoxygenation. For authentic hypoxic conditions, cells were cultured in a temperature-controlled hypoxia chamber (model CN-SQ110B, Chuanna, Shanghai, China) at 37 °C with 1% O_2 and 5% CO_2. For authentic reoxygenation, the cells were transferred to normal culture conditions with 21% O_2 and 5% CO_2 for continued incubation.

Reagents, antibodies, and plasmids

Reagents and antibodies used in this study include: YY1 (Abcam, cat. ab109237, 1:1000 for western blot (WB), 1:200 for immunofluorescent (IF) staining; Boster, cat. PB9909, 1:100 for IMC); YY1 (H-10) (Santa Cruz, cat. sc-7341, 1:50 for immunoprecipitation (IP), 1:200 for IF); NUSAP1 (Proteintech, cat. 12024-1-AP, 1:2000 for WB, 1:100 for IP, 1:200 for IF); HIF-1α (abcam, cat. ab51608, 1:1000 for WB, 1:500 for IF, 1:100 for IP; cat. ab210073, 1:150 for IMC); Lyn (Proteintech, cat. 18135-1-AP, 1:1000 for WB); and Tubulin (Proteintech, cat. 11224-1-ap, 1/2000 for WB); SUMO2/3 (Abcam, cat. ab81371, 1:1000 for WB, or Proteintech, cat. 11251-1-ap, 1:1000 for WB); Ubiquitin (Abcam, cat. ab134953, 1:1000 for WB, or Proteintech, cat. 10201-2-ap, 1:1000 for WB); Flag (Cell signaling Technology, cat. 14793S, 1:1000 for WB, 1:200 for IP); EGFP (Proteintech, cat. 66002-1-lg, 1:2000 for WB, 1:200 for IP); HA (Proteintech, cat. 51064-2-ap, 1:2000 for WB, 1:200 for IP); Phospho-Serine (Immunechem, cat. ICP9806, 1:250 for WB); Phospho-Tyrosine (Immunechem, cat. ICP9805, 1:250 for WB); Phospho-YY1 (Affinity, cat. AF3694, 1:1000 for WB); GAPDH (Acton, cat. 10R-G109A, 1:1000 for WB); F4/80 (Aifang biological, cat. SAF002, 1:500 for mIHC); Goat anti-mouse IgG-HRP (Santa Cruz, cat. sc2005,1:5000 for WB); CD68 (Biolegend, cat. 916104, 1:100 for IMC); Goat anti-rabbit IgG-HRP (Santa Cruz, cat. sc-2004, 1:5000 for WB); PE-CD8 (BD Bioscience, cat. 553030, 1:50 for FC); APC-CD3 (BD Bioscience, cat. 555275, 1:50 for FC); PE-CD274 (Biolegend, cat. 329706, 1:50 for FC); 1,6-hexanediol (Aladdin, cat. H103708); Tenapanor (TargetMol, T7587, cat. 1234423-95-0); MG132 (MACKLIN, cat. HY132-59); CHX (MACKLIN, cat. HY-12320, 100 μg/ml for CHX assay); Subasumstat (MACKLIN, TAK-981, cat. HY-111789); Na_3VO_4 (MACKLIN, cat. 13721-39-6); SU6656 (MACKLIN, cat. HY-B078); K3PO4 (MACKLIN, cat. NONE8222); Protein A/G Magnetic Beads (Beyotime, cat. P2108); Anlotinib (cat. AL3818) dihydrochloride (Aladdin, cat. 1360460-82-7); Cobalt Chloride Solution (MACKLIN, cat. 7791-13-1); anti-mouse PD-1 (Bio X Cell, cat. 857122D1); Anti-mouse lgG (Bio X Cell, cat. 84932331).

The full lengths of YY1, HIF-1α, and their mutants, as well as NUSAP1, were individually subcloned into a eukaryotic EGFP or mCherry expression vector (pcDNA3.1, Genscreat, Genechem, or Genewiz) for studying phase separation. A bacterial expression system was used to express these coding sequences, and recombinant proteins were purified using Ni-NTA agarose. The full-length and truncated coding sequences of YY1, HIF-1α, and NUSAP1 were also individually subcloned into eukaryotic expression vectors with N-terminal 3×HA-tag, 3×His-tag, and 3×Flag-tag at the N-terminus for studying protein binding. The project or cat. ID of vectors and reconstructions is listed in Supplementary Table 2.

Gene knockout system

siRNAs targeting YY1, HIF-1α, and NUSAP1 were constructed and purchased from GenePharma Co. (Shanghai, China). The sequences are listed in Supplementary Table 3.

RNA extraction and RT-PCR

An RNA extraction kit (Takara Kusatsu) was used for RNA extraction according to the manufacturer's protocol. cDNA was prepared by reverse transcription polymerase chain reaction (RT-PCR) from purified RNA with the Hiscript II First-Strand cDNA Synthesis Kit (Vazyme, cat. R212-01). Quantitative Real-time PCR was performed using the MonAmpTM SYBR Green qPCR Mix (Monad Biotech, cat. MQ10101S). The comparative threshold cycle method was used to calculate the relative gene expression levels by normalizing to the reference gene GAPDH.

Western blotting

Total protein was extracted from cells by using the RIPA lysis buffer (KeyGene Biotech, cat. KGB5203, 1:1000) according to the manufacturer's instructions. The protein concentration was determined with the bicinchoninic acid assay (BCA, KeyGene Biotech, cat. KGB2101). The protein was separated by sodium dodecyl sulfate-polyacrylamide (SDS) gel electrophoresis and transferred onto a polyvinylidene difluoride membrane (Merck Millipore, cat. SVLP04700). The membrane was then blocked for 1 h with 5% skimmed milk and incubated with the following primary antibodies overnight, followed by horseradish peroxidase (HRP) conjugated secondary antibodies. The unprocessed scans of blots from the figure displayed and replicated experiments were included in the Source Data file.

Immunoprecipitation-mass spectrometry (IP-MS) and coimmunoprecipitation assays (CO-IP)

For IP-MS assays, the Protein A/G was pre-incubated with the indicated YY1 or rabbit IgG (Proteintech, cat. B900610) for 4 h. The cell lysis supernatant was then incubated with antibody-coupled magnetic beads at 4 °C overnight. Elute with 0.1 M Glycine-HCl, pH 3.0, and neutralize with 0.5 M Tris-HCl, pH 7.4, 1.5 M NaCl for protein MS analysis (GeneChem). The list of YY1 IP-MS results was shown in Supplementary Data 1. For Co-IP assays, the extracts were immunoprecipitated with anti-Flag or anti-HA magnetic beads (Thermo Fisher Scientific, cat. 88802) overnight at 4 °C and boiled with SDS loading buffer. The released binding proteins were then eluted for western blotting analysis using the indicated antibodies.

Ubiquitination assay

Cells were incubated with proteasome inhibitor MG132 (Sigma-Aldrich, USA, cat. 1211877-36-9, 50 μg/mL) for 6 h in a 37 °C incubator and then lysed with IP lysis buffer. Lysates were then incubated with HIF-1α antibody (2 μg, Abcam, cat. ab51608, 1:100) as well as IgG (rabbit) coupled to protein A/G magnetic beads at 4 °C overnight to immunoprecipitate the HIF-1α proteins. After washing with PBS five times, proteins were denatured at 100 °C for 5 min and then separated by 10% SDS-PAGE. Ubiquitin antibody was used to detect the ubiquitination of HIF-1α.

SUMOylation assay

Cells were washed with cold wash buffer (10 mM NEM in PBS) and then lysed with lysis buffer (protease inhibitor and phosphatase inhibitor cocktails, Beyotime, cat. P1046). Cell lysates were sonicated until they became fluid and then diluted 1:10 with dilution buffer. Lysates were then incubated with anti-HIF-1α antibody (Abcam, cat. ab51608, 1:100) coupled to protein A/G magnetic beads at 4 °C overnight. Beads were boiled in SDS sample buffer. SUMOylated HIF-1α was detected by western blot using an anti-SUMO2/3 antibody.

RNA-sequencing analysis

Total RNA was extracted and quantified using NanoDrop ND-100 (Thermo Fisher Scientific), with 1–2 μg of RNA used for library construction. Libraries were prepared using the KAPA Stranded RNA-Seq Library Prep Kit (Illumina, USA, cat. 20040529) and sequenced on the Illumina NovaSeq 6000 platform. Mice subcutaneous tumor cells with NC/TEN-M2pep treatment were sorted for CD45-positive cells prior to RNA extraction and sequencing, and the differentially expressed genes are listed in Supplementary Data 2. Bioinformatics analysis included quality control, alignment to the reference genome using Hisat2, and differential expression analysis using Ballgown. Pathway enrichment analysis was conducted using the KEGG database to identify overrepresented biological pathways among the differentially expressed genes.

Immunofluorescence staining

Cells were seeded on glass coverslips in glass-bottom dish (φ14 mm) and cultured overnight. Subsequently, cells were fixed with the Immunol Staining Fix Solution (Beyotime, cat. P0098) for 30 min at room temperature. After blocking by 10% FBS for 30 min at room temperature, cells were incubated with a primary antibody for 30 min at room temperature. After washing thrice with PBS, cells were incubated with an Alex-Fluor-488 or 594-conjugated secondary antibody (Abcam, cat. ab150077 or ab150080) for 30 min at room temperature. Finally, after washing thrice with PBS, nuclei were counterstained with DAPI (Jiangsu KeyGEN BioTECH, cat. KGA215-50), and images were captured by a Fluoview FV3000 fluorescence confocal microscope (Olympus).

Cell imaging, phase separation, and fluorescence recovery after photobleaching (FRAP) assays

Cells were cultured in a glass-bottom dish. Before Cell imaging, the culture medium was exchanged for Opti-MEM. Images were acquired by a Fluoview FV3000 fluorescence confocal microscope with a 60× oil immersion lens. Fluorescence signals were obtained with excitation/emission at 488/546 nm for EGFP. The droplet fusion was recorded for 20–30 time points (200–300 s). The IDRs of YY1, NUSAP1, and HIF-1α proteins were predicted by the PONDR website, and the VSL2 algorithm was used in the prediction to obtain the disordered maps of the three proteins. The information of HIF-1α-IDR 1-EGFP (amino acids 1–80), HIF-1α-IDR2-EGFP (amino acids 391–750), HIF-1α-non-IDR-EGFP (amino acids 81–390), HIF-1α-whole-EGFP (amino acids 1–826), NUSAP1-whole-mCherry (amino acids 1–441) and YY1-whole-mCherry (amino acids 1–414) fusion protein was listed in the Supplementary Table 2. Potassium phosphate buffer (pH 7.0) was used for desalination of the fusion proteins. Polyethylene glycol (PEG) 8000 (30%), as a molecule crowder, together with desalted fusion protein forms solutions with different protein concentration gradients (1, 2, 5, 10, and 20 μM). The mixed solution was loaded onto glass slides with coverslips, followed by immediate visualization by a Fluoview FV1000 fluorescence confocal microscope.

The FRAP assay was performed on a Fluoview FV3000 fluorescence confocal microscope with a 60× oil immersion lens. The transfected 293T cells were cultured in a glass-bottom dish. Before FRAP, the culture medium was exchanged for Opti-MEM (Gibco, cat. 31985062). The droplets in cells were bleached for 3–5 s with 10–20% of the maximum laser power of a 488 nm laser (1 absorbance unit). The recovery was recorded for 20–30 time points after bleaching (200–300 s). The fluorescent intensity of the bleached area over time was calculated by Zen (Zeiss, Germany). During image acquisition, cells were incubated in a chamber at 37 °C supplied with 5% CO_2.

Mice tumorigenicity assay

C57BL/6 male mice (Changzhou Cavens Model Animal, China, stock No. C000101) were raised at the Animal Center of Southeast University, which contains a specific pathogen-free barrier laboratory. This facility is equipped with essential barrier components to ensure a controlled and sterile environment. These components include sterilized or disinfected equipment and supplies, steam-sterilized or irradiated feed and drinking water, and air-shower entry protocols. Experimental and control animals were co-housed under a 12-h light/dark cycle at 22 ± 2 °C with 50 ± 10% humidity to minimize environmental variability. Before the experiment, the mice were adapted to the laboratory environment for 2–3 weeks until 6–8 weeks old. All operations on experimental mice are performed under the supervision of the Animal Ethics Committee of Southeast University. RM-1 cells (5×10^6) alone or ones mixed with RAW264.7 cells (5×10^6) transfected with si/nc-YY1, were injected subcutaneously on the back of mice. M2pep (peptide YEQDPWGVKWWY)[38], which was synthesized by RuixiBio (Xi'an, China), was modified on a liposome carrier and loaded with Tenapanor or control solvent to construct TEN-M2pep or NC-M2pep. In the in vivo therapeutic experiments, TEN-M2pep or NC-M2pep were injected intravenously 1 week after the subcutaneous tumor construction. Tumor volume was evaluated twice a week after injection, following the formula of length × width^2/2.

All animal experimental protocols were approved by the Ethics Committee of Zhongda Hospital, Southeast University, and conducted following the National Guidelines for the Health Use of Laboratory Animals (Approval ID: 20220225034). The ethical board permits subcutaneous tumors to reach a size not exceeding 10% of the animal's body weight, or until tumors become ulcerated. For instance, the maximum diameter of a subcutaneous tumor should be capped at 20 mm in a 20 g mouse and 25 mm in a 250 g rat. When tumor size measurement is not feasible, the criteria for determining the early

endpoint of animal experiments—namely, the conditions warranting euthanasia—are as follows: animals nearing death, unable to move, or unresponsive to gentle stimulation; those experiencing respiratory distress; animals with diarrhea or urinary incontinence; those that have lost 20% or more of their initial body weight; animals unable to eat or drink; those displaying significant anxiety or restlessness; animals with paralysis, persistent seizures, or stereotypic behavior; animals with skin damage covering over 30% of their body or showing signs of infection; and any other conditions deemed by a veterinarian to necessitate euthanasia. In accordance with the ethical guidelines, the approved method for euthanizing mice in this study involves initial anesthesia with isoflurane followed by carbon dioxide inhalation. Throughout the research, we rigorously adhered to the established early endpoints for animal experiments and the specified euthanasia protocol.

Flow cytometry

Fresh tissue was cut into pieces and cultured in Collagenase IV and DNase I for 30 min at room temperature. To quantify the cell subgroup and the expression of molecules on the cells, the purified single-cell suspensions were blocked with mouse FcR blocking reagent (Miltenyi Biotec, cat. 130-092-575) for 10 min at 4 °C prior to surface staining. Purified cells were stained with PE-CD8 (Biolegend, cat. 100707) and APC-CD3 (Biolegend, cat. 100236) at 4 °C for 30 min. Dead cells were excluded with eFluor506 (eBioscience, cat. 65-0866-14) or Propidium Iodide (PI, Sigma-Aldrich, cat. 25535-16-4), and the immune cells were gated based on the expression of CD45. The gates of positive cells for each dye were set based on single-stained cells and isotype controls. FC analysis was performed using a FACS flow cytometer (BD Biosciences) and analyzed by FlowJo V10 (TreeStar).

Fabrication of YY1-DbTACs and M2pep-YY1-DbTACs

All DNA strands were purchased from Biolink Biotechnology. Single-stranded DNA S1 (1000 μL, 50 μM) was mixed with CRBN ligand solution (50 μL, 1000 μM). The solution was shaken for 2 h (37 °C, 21 × *g*). Subsequently, the mixture was combined with pre-designed single-stranded DNA S2 (1:1 molar ratio). The resulting solution was heated for 5 min (95 °C) using a T-series multi-block thermal cycler (LongGene), then annealed for 30 min (4 °C), resulting in the YY1-DbTACs structure. Finally, the prepared YY1-DbTACs were stored at 4 °C.

The formulation of YY1-DbTACs liposome was crafted via a streamlined thin-film hydration approach. We started by dissolving 25 mg of soybean phosphatidylcholine, 5 mg of cholesterol hemisuccinate (CHEMS), and 2 mg of YY1-DbTACs in an ethanol-dichloromethane mixture. Post solvent removal, the film was hydrated in 5 mL PBS at 37 °C for 30 min. The liposomes were then subjected to ultrasonication at 100 W for 30 min to ensure uniformity. To refine the preparation, we performed centrifugation using an ultrafiltration tube at 1800 × *g* for 20 min at 4 °C to eliminate unencapsulated drug. The final step involved a 1-h incubation with an M2 peptide (DSPE-PEG2000-YEQDPWGVKWWY) to achieve the desired product.

Fabrication, self-assembly and stability of YY1-targeted tetrahedral DNA-caged PROTACs (YY1-DcTACs)

For YY1-DcTACs, single-stranded DNA S2 (1000 μL, 50 μM) was mixed with a solution of CRBN ligand (50 μL, 1000 μM). The solution was shaken for 2 h (37 °C, 21 × *g*). Subsequently, the mixture was combined with the pre-designed single-stranded DNA sequences S1, S3, and S4 in a 1:1:1:1 molar ratio (Supplementary Table 3). The resulting solution was heated for 10 min (95 °C) using a PCR machine (LongGene) and then annealed for 35 min (4 °C) to obtain the YY1-DcTACs structure. Finally, the prepared YY1-DcTACs were stored at 4 °C.

To verify the covalent binding of ligands and the principle of stepwise self-assembly of YY1-DcTACs, a PAGE (10%) gel was employed. 5 μL of each sample were mixed with 1 μL of DNA loading buffer (6×). Electrophoresis was conducted in 1× TBE-Mg^{2+} buffer at 120 V for 70 min. The gel was stained with SYBR Green (10,000×, Solarbio Science & Technology, cat. SY1020) in the dark for 0.5 h, and then the images were captured using a Bio-Rad Gel Doc EZ Imager (Hercules). YY1-DcTACs (2 μM) were mixed with PBS and IMDM medium containing 10% FBS, and incubated at 37 °C. Samples were collected at various time points (1, 2, 4, 6, 12, 24 h) and analyzed for the stability of YY1-DcTACs using 10% PAGE gel electrophoresis.

Response efficiency of YY1-DcTACs

The YY1-DcTACs solution was mixed with the complementary RNA strand S1 in equal molar ratios and incubated at 37 °C for 6 h. The samples were then collected and analyzed using 10% PAGE gel electrophoresis and fluorescence spectrophotometer detection. To differentiate RAW264.7 cells into M0 macrophages, we incubated them with 100 ng/mL phorbol 12-myristate 13-acetate (PMA, Sigma-Aldrich, cat. 16561-29-8) for 48 h. M0 macrophages were induced into M2 macrophages using 20 ng/mL of IL-4 (20 ng/mL, Beyotime, cat. P5916) and IL-10 (20 ng/mL, Beyotime, cat. P5939) for 24 h, and into M1 macrophages with LPS (100 ng/mL, Sigma-Aldrich, cat. 93572-42-0) and IFN-γ (20 ng/mL, Beyotime, cat. P6137) for 24 h. Prior to proceeding with the subsequent experiments, qPCR was employed to detect M2 markers (ARG1 and IL-10) and M1 markers (iNOS, TNF-α) to confirm the successful induction. Macrophages of types M0, M1, and M2, normal hepatocytes L02, and cancer cells were cultured in confocal dishes at a density of 1×10^5 cells per dish. 200 μL of 1 μM YY1-DcTACs was added to each dish, and the cells were incubated at 37 °C under 5% CO_2 for 6 h. The culture medium was discarded, and the cells were washed three times with cold PBS buffer for 30 s. The cells were then fixed with 4% paraformaldehyde at room temperature, followed by three washes with cold PBS buffer for 5 min. The cell nuclei were stained with DAPI (1 μg/mL, Jiangsu KeyGEN BioTECH, cat. KGA215-50) for 10 min at room temperature and washed. Images were acquired using a confocal laser scanning microscope (FV1000, Olympus).

Single-cell RNA sequencing (scRNA-seq) of YY1-DcTACs-treated subcutaneous tumors

Subcutaneous tumors harvested from mice treated with either NC/YY1-DcTACs were dissociated into single-cell suspensions using SeekMate Tissue Dissociation Reagent Kit A Pro (SeekGene, cat. K01801-30) at 37 °C. Following erythrocyte lysis with an erythrocyte removal reagent (Solarbio, cat. R1010), cell count and viability were assessed using the SeekMate Tinitan Fluorescence Cell Counter (SeekGene, M002C) with AO/PI reagent. Based on the results, the debris and dead cells were removed using a cell strainer and dead cell removal kit (Miltenyi, cat. 130-109-398 and cat. 130-090-101). Subsequently, $CD45^+$ cells were magnetically labeled and isolated with CD45 MicroBeads (mouse, Miltenyi, cat. 130-052-301) and mixed with the $CD45^-$ cells at a 6:4 ratio. The cells were then washed twice in RPMI 1640 medium and resuspended at a concentration of 1×10^6 cells/ml. Single-cell libraries were prepared using the SeekOne Digital Droplet Single-Cell 3′ library preparation kit (SeekGene cat. K00202) following the manufacturer's instructions. These libraries were sequenced on an Illumina NovaSeq X Plus platform, generating 150 bp paired-end reads. The raw sequencing data was processed by Fastp[65] firstly to trim primer sequences and low-quality bases. Subsequently, the Seeksoul tools (SeekGene, v1.2.1) were employed to demultiplex cellular barcodes and map reads to the mouse reference genome, generating a feature-barcode matrix. This matrix was then used for downstream analyses, such as converting the data into a Seurat object using the R package Seurat.

Construction of transgenic mice

In-Fusion cloning method was used to construct a homologous recombinant donor vector, which was verified by enzyme digestion. C57BL/6J-$YY1^{em1Cflox}$ mice were constructed under the following steps[66].

Cas9 mRNA, gRNA, and donor vector were injected into the fertilized eggs of C57BL/6J mice by microinjection operating system to obtain F0 generation mice. F1 hybrid mice ($YY1^{flox/+}$, Aniphe Biolaboratory, stock No. AB000111) were then obtained by mating F0 mice with C57BL/6J mice. Breeding of $YY1^{flox/+}$ mice is carried out through both self-crossing and hybridization with Lyz2-Cre mice (JAX Mice, stock No. 004781), resulting in obtaining flox homozygous mice ($YY1^{flox/flox}$) and flox heterozygous Lyz2-Cre double-positive mice ($YY1^{flox/+:\ Cre+}$). Homozygous mice were mated with double-positive mice, and finally, the target mice with flox homozygous Lyz2-Cre positive genotype ($YY1^{flox/flox:\ Cre+}$) were obtained.

Statistics and reproducibility

All experiments were repeated three times independently, and a two-tailed Student's *t*-test or one-way ANOVA was used to compare the results in the research groups. All statistical analysis was carried out by SPSS software version 16.0, and $p < 0.05$ indicated that there was a statistically significant difference. The displayed Western blots, gels, and fluorescence images were selected as representative images from three independent replicate experiments.

Reporting summary

Further information on research design is available in the Nature Portfolio Reporting Summary linked to this article.

Data availability

All data are included in the Supplementary Information or available from the authors, as are unique reagents used in this article. Source data are provided with this paper. The raw numbers for charts and graphs are available in the Source Data file whenever possible. The data of YY1 IP-MS generated in this study have been deposited in the database of Dyrad under a https://doi.org/10.5061/dryad.rr4xgxdkn. The raw data of RNA-seq reported in this paper have been deposited in the Genome Sequence Archive[67] in the National Genomics Data Center[68], China National Center for Bioinformation/Beijing Institute of Genomics, Chinese Academy of Sciences (GSA: CRA027146). The third-party RNA-seq data (GSE16099) is available [https://www.ncbi.nlm.nih.gov/geo/query/acc.cgi?acc=GSE16099]. Source data are provided with this paper.

References

1. Bergengren, O. et al. 2022 update on prostate cancer epidemiology and risk factors—a systematic review. *Eur. Urol.* **84**, 191–206 (2023).
2. Cai, M. et al. Current therapy and drug resistance in metastatic castration-resistant prostate cancer. *Drug Resist. Updates* **68**, 100962 (2023).
3. Sharma, P. & Allison, J. P. Immune checkpoint targeting in cancer therapy: toward combination strategies with curative potential. *Cell* **161**, 205–214 (2015).
4. Zou, W., Wolchok, J. D. & Chen, L. PD-L1 (B7-H1) and PD-1 pathway blockade for cancer therapy: mechanisms, response biomarkers, and combinations. *Sci. Transl. Med.* **8**, 328rv324 (2016).
5. Sridaran, D. et al. Prostate cancer immunotherapy: improving clinical outcomes with a multi-pronged approach. *Cell Rep. Med.* **4**, 101199 (2023).
6. Wu, Q. et al. Hypoxia-inducible factors: master regulators of hypoxic tumor immune escape. *J. Hematol. Oncol.* **15**, 77 (2022).
7. Liikanen, I. et al. Hypoxia-inducible factor activity promotes antitumor effector function and tissue residency by CD8+ T cells. *J. Clin. Investig.* **131**, e143729 (2021).
8. Vito, A., El-Sayes, N. & Mossman, K. Hypoxia-driven immune escape in the tumor microenvironment. *Cells* **9**, 992 (2020).
9. Taylor, C. T. & Scholz, C. C. The effect of HIF on metabolism and immunity. *Nat. Rev. Nephrol.* **18**, 573–587 (2022).
10. Kopecka, J. et al. Hypoxia as a driver of resistance to immunotherapy. *Drug Resist. Updates* **59**, 100787 (2021).
11. Bai, R. et al. The hypoxia-driven crosstalk between tumor and tumor-associated macrophages: mechanisms and clinical treatment strategies. *Mol. Cancer* **21**, 177 (2022).
12. Caronni, N. et al. IL-1beta(+) macrophages fuel pathogenic inflammation in pancreatic cancer. *Nature* **623**, 415–422 (2023).
13. Yamaguchi, Y. et al. PD-L1 blockade restores CAR T cell activity through IFN-gamma-regulation of CD163+ M2 macrophages. *J. Immunother. Cancer* **10**, e004400 (2022).
14. Hornburg, M. et al. Single-cell dissection of cellular components and interactions shaping the tumor immune phenotypes in ovarian cancer. *Cancer Cell* **39**, 928–944.e6 (2021).
15. Sumitomo, R. et al. M2 tumor-associated macrophages promote tumor progression in non-small-cell lung cancer. *Exp. Ther. Med.* **18**, 4490–4498 (2019).
16. Li, T. J. et al. SIGLEC15 amplifies immunosuppressive properties of tumor-associated macrophages in pancreatic cancer. *Cancer Lett.* **530**, 142–155 (2022).
17. Erlandsson, A. et al. M2 macrophages and regulatory T cells in lethal prostate cancer. *Prostate* **79**, 363–369 (2019).
18. Quaranta, V. et al. Macrophage-derived granulin drives resistance to immune checkpoint inhibition in metastatic pancreatic cancer. *Cancer Res.* **78**, 4253–4269 (2018).
19. Li, X. et al. Harnessing tumor-associated macrophages as aids for cancer immunotherapy. *Mol. Cancer* **18**, 177 (2019).
20. Li, T., Zeng, Z., Fan, C. & Xiong, W. Role of stress granules in tumorigenesis and cancer therapy. *Biochim. Biophys. Acta Rev. Cancer* **1878**, 189006 (2023).
21. Ambadipudi, S., Biernat, J., Riedel, D., Mandelkow, E. & Zweckstetter, M. Liquid-liquid phase separation of the microtubule-binding repeats of the Alzheimer-related protein Tau. *Nat. Commun.* **8**, 275 (2017).
22. Liu, D. et al. IFI16 phase separation via multi-phosphorylation drives innate immune signaling. *Nucleic Acids Res.***51**, 6819–6840 (2023).
23. Wang, G. Z. & Goff, S. P. Regulation of Yin Yang 1 by tyrosine phosphorylation. *J. Biol. Chem.* **290**, 21890–21900 (2015).
24. Verheul, T. C. J., van Hijfte, L., Perenthaler, E. & Barakat, T. S. The Why of YY1: mechanisms of transcriptional regulation by Yin Yang 1. *Front. Cell Dev. Biol.* **8**, 592164 (2020).
25. Wang, W. et al. A histidine cluster determines YY1-compartmentalized coactivators and chromatin elements in phase-separated enhancer clusters. *Nucleic Acids Res.* **50**, 4917–4937 (2022).
26. Noman, M. Z. et al. PD-L1 is a novel direct target of HIF-1alpha, and its blockade under hypoxia enhanced MDSC-mediated T cell activation. *J. Exp. Med.* **211**, 781–790 (2014).
27. Cubillos-Zapata, C. et al. Hypoxia-induced PD-L1/PD-1 crosstalk impairs T-cell function in sleep apnoea. *Eur. Respir. J.* **50**, 1700833 (2017).
28. Majmundar, A. J., Wong, W. J. & Simon, M. C. Hypoxia-inducible factors and the response to hypoxic stress. *Mol. Cell* **40**, 294–309 (2010).
29. Masson, N., Willam, C., Maxwell, P. H., Pugh, C. W. & Ratcliffe, P. J. Independent function of two destruction domains in hypoxia-inducible factor-alpha chains activated by prolyl hydroxylation. *EMBO J.* **20**, 5197–5206 (2001).
30. Hoege, C., Pfander, B., Moldovan, G. L., Pyrowolakis, G. & Jentsch, S. RAD6-dependent DNA repair is linked to modification of PCNA by ubiquitin and SUMO. *Nature* **419**, 135–141 (2002).
31. Zhao, Y., He, J., Li, Y., Lv, S. & Cui, H. NUSAP1 potentiates chemoresistance in glioblastoma through its SAP domain to stabilize ATR. *Signal Transduct. Target. Ther.* **5**, 44 (2020).

32. Zheng, H. et al. Comprehensive pan-cancer analysis reveals NUSAP1 is a novel predictive biomarker for prognosis and immunotherapy response. *Int. J. Biol. Sci.* **19**, 4689–4708 (2023).
33. Mills, C. A. et al. Nucleolar and spindle-associated protein 1 (NUSAP1) interacts with a SUMO E3 ligase complex during chromosome segregation. *J. Biol. Chem.* **292**, 17178–17189 (2017).
34. Yao, Y. L., Yang, W. M. & Seto, E. Regulation of transcription factor YY1 by acetylation and deacetylation. *Mol. Cell. Biol.* **21**, 5979–5991 (2001).
35. Vertegaal, A. C. O. Signalling mechanisms and cellular functions of SUMO. *Nat. Rev. Mol. Cell Biol.* **23**, 715–731 (2022).
36. Wei, M., Huang, X., Liao, L., Tian, Y. & Zheng, X. SENP1 decreases RNF168 phase separation to promote DNA damage repair and drug resistance in colon cancer. *Cancer Res.* **83**, 2908–2923 (2023).
37. Pergola, P. E., Rosenbaum, D. P., Yang, Y. & Chertow, G. M. A Randomized trial of tenapanor and phosphate binders as a dual-mechanism treatment for hyperphosphatemia in patients on maintenance dialysis (AMPLIFY). *J. Am. Soc. Nephrol.* **32**, 1465–1473 (2021).
38. Cieslewicz, M. et al. Targeted delivery of proapoptotic peptides to tumor-associated macrophages improves survival. *Proc. Natl. Acad. Sci. USA* **110**, 15919–15924 (2013).
39. Hosea, R., Hillary, S., Wu, S. & Kasim, V. Targeting transcription factor YY1 for cancer treatment: current strategies and future directions. *Cancers* **15**, 3506 (2023).
40. Li, K. & Crews, C. M. PROTACs: past, present and future. *Chem. Soc. Rev.* **51**, 5214–5236 (2022).
41. Zhou, L. et al. DNA framework-engineered chimeras platform enables selectively targeted protein degradation. *Nat. Commun.* **14**, 4510 (2023).
42. Atchison, M., Basu, A., Zaprazna, K. & Papasani, M. Mechanisms of Yin Yang 1 in oncogenesis: the importance of indirect effects. *Crit. Rev. Oncog.* **16**, 143–161 (2011).
43. Gordon, S., Akopyan, G., Garban, H. & Bonavida, B. Transcription factor YY1: structure, function, and therapeutic implications in cancer biology. *Oncogene* **25**, 1125–1142 (2006).
44. Meliala, I. T. S., Hosea, R., Kasim, V. & Wu, S. The biological implications of Yin Yang 1 in the hallmarks of cancer. *Theranostics* **10**, 4183–4200 (2020).
45. Wu, S. et al. Transcription factor YY1 promotes cell proliferation by directly activating the pentose phosphate pathway. *Cancer Res.* **78**, 4549–4562 (2018).
46. Chen, S. et al. YY1 complex in M2 macrophage promotes prostate cancer progression by upregulating IL-6. *J. Immunother. Cancer* **11**, e006020 (2023).
47. Shin, Y. & Brangwynne, C. P. Liquid phase condensation in cell physiology and disease. *Science* **357**, eaaf4382 (2017).
48. Ahn, J. H. et al. Phase separation drives aberrant chromatin looping and cancer development. *Nature* **595**, 591–595 (2021).
49. Wang, J. et al. A molecular grammar governing the driving forces for phase separation of prion-like RNA binding proteins. *Cell* **174**, 688–699.e16 (2018).
50. Zhao, M. et al. GCG inhibits SARS-CoV-2 replication by disrupting the liquid phase condensation of its nucleocapsid protein. *Nat. Commun.* **12**, 2114 (2021).
51. Her, C. et al. Molecular interactions underlying the phase separation of HP1alpha: role of phosphorylation, ligand and nucleic acid binding. *Nucleic Acids Res.* **50**, 12702–12722 (2022).
52. Jang, Y., Kang, S., Han, H. H., Kim, B. G. & Cho, N. H. CD24 induced cellular quiescence-like state and chemoresistance in ovarian cancer cells via miR-130a/301a-dependent CDK19 downregulation. *Cell Death Discov.* **10**, 81 (2024).
53. Wei, S. Y. et al. Endothelial Yin Yang 1 phosphorylation at S118 induces atherosclerosis under flow. *Circ. Res.* **129**, 1158–1174 (2021).
54. Jaakkola, P. et al. Targeting of HIF-alpha to the von Hippel-Lindau ubiquitylation complex by O_2-regulated prolyl hydroxylation. *Science* **292**, 468–472 (2001).
55. Bononi, A. et al. BAP1 is a novel regulator of HIF-1alpha. *Proc. Natl. Acad. Sci. USA* **120**, e2217840120 (2023).
56. Li, K. et al. The SUMOylation and ubiquitination crosstalk in cancer. *J. Cancer Res. Clin. Oncol.* **149**, 16123–16146 (2023).
57. Carbia-Nagashima, A. et al. RSUME, a small RWD-containing protein, enhances SUMO conjugation and stabilizes HIF-1alpha during hypoxia. *Cell* **131**, 309–323 (2007).
58. Li, J. et al. Cbx4 governs HIF-1alpha to potentiate angiogenesis of hepatocellular carcinoma by its SUMO E3 ligase activity. *Cancer Cell* **25**, 118–131 (2014).
59. Raemaekers, T. et al. NuSAP, a novel microtubule-associated protein involved in mitotic spindle organization. *J. Cell Biol.* **162**, 1017–1029 (2003).
60. Zheng, M. et al. MITF regulates the subcellular location of HIF1alpha through SUMOylation to promote the invasion and metastasis of daughter cells derived from polyploid giant cancer cells. *Oncol. Rep.* **51**, 63 (2024).
61. Lin, X. et al. Sumoylation enhances the activity of the TGF-beta/SMAD and HIF-1 signaling pathways in keloids. *Life Sci.* **255**, 117859 (2020).
62. Bekes, M., Langley, D. R. & Crews, C. M. PROTAC targeted protein degraders: the past is prologue. *Nat. Rev. Drug Discov.* **21**, 181–200 (2022).
63. Du, J. et al. Selective oxidative protection leads to tissue topological changes orchestrated by macrophage during ulcerative colitis. *Nat. Commun.* **14**, 3675 (2023).
64. Hoch, T. et al. Multiplexed imaging mass cytometry of the chemokine milieus in melanoma characterizes features of the response to immunotherapy. *Sci. Immunol.* **7**, eabk1692 (2022).
65. Chen, S., Zhou, Y., Chen, Y. & Gu, J. fastp: an ultra-fast all-in-one FASTQ preprocessor. *Bioinformatics* **34**, i884–i890 (2018).
66. Yin, H. et al. RNA m6A methylation orchestrates cancer growth and metastasis via macrophage reprogramming. *Nat. Commun.* **12**, 1394 (2021).
67. Chen, T. et al. The genome sequence archive family: toward explosive data growth and diverse data types. *Genom. Proteom. Bioinform.* **19**, 578–583 (2021).
68. CNCB-NGDC Members and Partners Database Resources of the National Genomics Data Center, China National Center for Bioinformation in 2025. *Nucleic Acids Res.* **53**, D30–D44 (2025).

Acknowledgements

We are grateful to the staff of the Public Scientific Research Platform of Zhongda Hospital, Southeast University, and the Cultivation and Construction Site of the State Key Laboratory of Intelligent Imaging and Interventional Medicine (Southeast University) for technical assistance. The doctoral students in this project were under the support of Southeast University Innovation Capability Enhancement Plan for Doctoral Students, and the study was supported by the Open Research Fund of State Key Laboratory of Digital Medical Engineering, and the financially supported by the following funding: National Natural Science Foundation of China 92359304 (S.J.), Fundamental Research Funds for the Central Universities 2242023K5007 (B.X.), General social development project of Jiangsu Science and Technology Department BE2023771 (B.X.), China Postdoctoral Science Foundation funded project 2023M730572 (W.L.), Outstanding Youth Foundation of Jiangsu Province of China BK20220150 (Y.M.), Open Research Fund of State Key Laboratory of Digital Medical Engineering 2023-K10 (B.X.), Jiangsu Province High-Level Hospital Construction Funds of Zhongda Hospital GSP-JCYJ05 (B.X.), GSP-LCYJFH11 (W.L.), Top Talent Support Program for young and middle-aged people of Wuxi Health Committee HB2023117 (M.Z.).

Author contributions

Conceptualization: B.X., S.J., M.C. Methodology: W.L., S.C., Y.M., R.N., C.C., C.S., Y.H., X.Y. Investigation: J.L., W.M., S.Z., M.Z., Z.C., R.N. Visualization: W.L., T.W., Y.C., Y.H., N.S. Clinical samples collection: S.Z., K.L., L.H.Z. (Lihua Zhang), L.Z. (Lei Zhang). Funding acquisition: B.X., S.J., Y.M., W.L., M.Z. Project administration: B.X., M.C. Supervision: B.X., S.J., D.Z. Writing—original draft: W.L., Y.M., S.C. Writing—review and editing: B.X., S.J., J.L., W.M., S.Z., M.Z., D.Z.

Competing interests

The authors declare no competing interests.

Ethics approval

All human tumor tissue samples were collected in accordance with the national and institutional ethical guidelines. The study design was approved by the Ethics Committee of Zhongda Hospital, Southeast University. The approval ID is 2022ZDKYSB099. All animal experimental protocols were approved by the Ethics Committee of Zhongda Hospital, Southeast University, and conducted following the National Guidelines for the Health Use of Laboratory Animals. The approval ID is 20220225034.

Additional information

Supplementary information The online version contains supplementary material available at https://doi.org/10.1038/s41467-025-61560-0.

Correspondence and requests for materials should be addressed to Shenghong Ju, Dingxiao Zhang, Yi Ma or Bin Xu.

Peer review information *Nature Communications* thanks Giuseppina Carbone, who co-reviewed with Elisa Federici, Osamu Takeuchi, and the other anonymous reviewer(s) for their contribution to the peer review of this work. A peer review file is available.

[1]Department of Urology, Zhongda Hospital, Medical School, Southeast University, Nanjing, China. [2]Division of Life Sciences and Medicine, Department of Urology, The First Affiliated Hospital of USTC, University of Science and Technology of China, Hefei, China. [3]Center of Interventional Radiology & Vascular Surgery, Department of Radiology, Zhongda Hospital, Medical School, Southeast University, Nanjing, China. [4]Department of Oncology, Zhongda Hospital, Southeast University, Nanjing, China. [5]Department of Urology, Xishan People's Hospital of Wuxi City, Wuxi, China. [6]Department of Pathology, Zhongda Hospital, Southeast University, Nanjing, China. [7]Department of Bioinformatics, School of Biomedical Engineering and Informatics, Nanjing Medical University, Nanjing, China. [8]Key Laboratory of Biomedical Information Engineering of Ministry of Education, Biomedical Informatics & Genomics Center, School of Life Science and Technology, Xi'an Jiaotong University, Xi'an, China. [9]Nurturing Center of Jiangsu Province for State Laboratory of AI Imaging & Interventional Radiology, Department of Radiology, Zhongda Hospital, Medical School, Southeast University, Nanjing, China. [10]Department of Urology, Northern Jiangsu People's Hospital, Yangzhou, China. [11]Department of Urology, The First Affiliated Hospital of Bengbu Medical University, Bengbu, China. [12]Department of Surgery, LKS School of Medicine, The University of Hong Kong, Hong Kong, China. [13]School of Biomedical Sciences, Hunan University, Changsha, China. [14]Department of Biomedical Engineering, School of Engineering, China Pharmaceutical University, Nanjing, China. [15]National Innovation Platform for Integration of Medical Engineering Education (NMEE), Basic Medicine Research and Innovation Center (Ministry of Education), Southeast University, Nanjing, China. [16]These authors contributed equally: Wenchao Li, SaiSai Chen, Jian Lu, Weipu Mao, Shiya Zheng, Minhao Zhang. [17]These authors jointly supervised this work: Rong Na, Ming Chen. ✉e-mail: jsh@seu.edu.cn; zdx1980@hnu.edu.cn; yima@cpu.edu.cn; njxbseu@seu.edu.cn